

The growth and expansive applications of amorphous Ga_2O_3

Zhao-Ying Xi(奚昭颖), Li-Li Yang(杨莉莉), Lin-Cong Shu(舒林聪), Mao-Lin Zhang(张茂林), Shan Li(李山), Li Shi(史丽), Zeng Liu(刘增), Yu-Feng Guo(郭宇锋), and Wei-Hua Tang(唐为华)

Citation: Chin. Phys. B, 2023, 32 (**8**): 088502. DOI: 10.1088/1674-1056/accf81
Journal homepage: http://cpb.iphy.ac.cn; http://iopscience.iop.org/cpb

What follows is a list of articles you may be interested in

A non-quasi-static model for nanowire gate-all-around tunneling field-effect transistors

Bin Lu(芦宾), Xin Ma(马鑫), Dawei Wang(王大为), Guoqiang Chai(柴国强),Linpeng Dong(董林鹏), and Yuanhao Miao(苗渊浩)

Chin. Phys. B, 2023, 32 (**6**): 068501. DOI: 10.1088/1674-1056/acbe32

One ε-Ga_2O_3-based solar-blind Schottky photodetector emphasizing high photocurrent gain and photocurrent-intensity linearity

Yue-Hua An(安跃华), Zhen-Sen Gao(高震森), Yu Guo(郭雨), Shao-Hui Zhang(张少辉), Zeng Liu(刘增), and Wei-Hua Tang(唐为华)

Chin. Phys. B, 2023, 32 (**5**): 058502. DOI: 10.1088/1674-1056/acb75b

Optimal impurity distribution model and experimental verification of variation of lateral doping termination

Min Ren(任敏), Chang-Yu Ye(叶昶宇), Jian-Yu Zhou(周建宇), Xin Zhang(张新), Fang Zheng(郑芳), Rong-Yao Ma(马荣耀), Ze-Hong Li(李泽宏), and Bo Zhang(张波)

Chin. Phys. B, 2023, 32 (**4**): 048505. DOI: 10.1088/1674-1056/acbd29

Dynamic electrostatic-discharge path investigation relied on different impact energies in metal-oxide-semiconductor circuits

Tian-Tian Xie(谢田田), Jun Wang(王俊), Fei-Bo Du(杜飞波), Yang Yu(郁扬), Yan-Fei Cai(蔡燕飞), Er-Yuan Feng(冯二媛), Fei Hou(侯飞), and Zhi-Wei Liu(刘志伟)

Chin. Phys. B, 2023, 32 (**4**): 048501. DOI: 10.1088/1674-1056/ac9607

High performance carrier stored trench bipolar transistor with dual shielding structure

Jin-Ping Zhang(张金平), Hao-Nan Deng(邓浩楠), Rong-Rong Zhu(朱镕镕), Ze-Hong Li(李泽宏), and Bo Zhang(张波)

Chin. Phys. B, 2023, 32 (**3**): 038501. DOI: 10.1088/1674-1056/ac873d

---

REVIEW

The growth and expansive applications of amorphous Ga_2O_3

Zhao-Ying Xi(奚昭颖)[1], Li-Li Yang(杨莉莉)[1,2,†], Lin-Cong Shu(舒林聪)[1], Mao-Lin Zhang(张茂林)[1,2], Shan Li(李山)[1,2], Li Shi(史丽)[3], Zeng Liu(刘增)[1,2,4,‡], Yu-Feng Guo(郭宇锋)[1,2], and Wei-Hua Tang(唐为华)[1,2,§]

[1] *Innovation Center for Gallium Oxide Semiconductor (IC-GAO), College of Integrated Circuit Science and Engineering, Nanjing University of Posts and Telecommunications, Nanjing* 210023, *China*

[2] *National and Local Joint Engineering Laboratory for RF Integration and Micro-Assembly Technologies, Nanjing University of Posts and Telecommunications, Nanjing* 210023, *China*

[3] *Key Laboratory for Organic Electronics and Information Displays (KLOEID) & Institute of Advanced Materials (IAM), Jiangsu Key Laboratory for Biosensors, Jiangsu National Synergetic Innovation Center for Advanced Materials (SICAM), Nanjing University of Posts and Telecommunications, Nanjing* 210023, *China*

[4] *Key Laboratory of Aerospace Information Materials and Physics, Nanjing University of Aeronautics and Astronautics, Ministry of Industry and Information Technology, Nanjing* 211106, *China*

(Received 4 April 2023; revised manuscript received 20 April 2023; accepted manuscript online 24 April 2023)

As a promising ultra-wide bandgap semiconductor material, gallium oxide (Ga_2O_3) is attracting extensive attention of researchers due to its feasible growth process, appropriate bandgap of 4.4 eV–5.3 eV allowing for deep-ultraviolet (deep-UV) detection, good physical and chemical stability, high breakdown field strength and electron mobility, etc. Different from the strict processes for controllable crystalline Ga_2O_3 (usually refer to as stable monoclinic β-Ga_2O_3), amorphous Ga_2O_3 (a-Ga_2O_3) film can be prepared uniformly at low temperature on a large-area deposition substrate, suggesting great advantages such as low manufacturing cost and excellent flexibility, dispensing with high-temperature and high vacuum techniques. Thus, a-Ga_2O_3 extremely facilitates important applications in various applied fields. Therefore, in this concise review, we summarize several major deposition methods for a-Ga_2O_3 films, of which the characteristics are discussed. Additionally, potential methods to optimize the film properties are proposed by right of the inspiration from some recent studies. Subsequently, the applications of a-Ga_2O_3 thin films, e.g., in photodetectors, resistive random access memories (RRAMs) and gas sensors, are represented with a fruitful discussion of their structures and operating mechanisms.

Keywords: amorphous-Ga_2O_3, thin film, functional application

PACS: 85.30.De, 47.54.Jk **DOI:** 10.1088/1674-1056/accf81

1. Introduction

The study of amorphous materials has gone through a long way. In 1960s, Ovshinsky[1] published a patent for a switching device based on chalcogenide thin-film, which thrusts amorphous semiconductors into the limelight. In 1975, Speer *et al.*[2] realized the doping effect in amorphous silicon prepared by silane glow-discharge decomposition, making it possible to control the conductivity of amorphous semiconductors and manufacture p–n junctions based on them, opening the way for the application of amorphous semiconductors. In 1977, Mott and Anderson[3–5] were awarded the Nobel Prize in Physics for establishing the electronic theory of amorphous semiconductors and laid a theoretical foundation for the research of amorphous semiconductors. Amorphous semiconductors differ from crystalline semiconductors in optical and electrical properties mainly for their short range ordered and long-range disordered structures, as shown in Fig. 1. In the disordered system of amorphous semiconductors, the wave function of electrons is no longer the Bloch function (a solution of the Schrödinger equation for electrons moving in a periodic potential field), but it can be divided into extended states and localized states. The extended state wave function covers the whole material, which is similar to crystalline semiconductors. While, the disordered structure will lead to strong scattering, and its wave function will decay exponentially with the increase of distance. For this reason, the wave function will in a localized state. The electrons in the localized state need the assistance of phonons to achieve hopping conductance.[6–8] In addition, there exists a large number of defects in amorphous semiconductors, mainly vacancies, thus a series of defect energy levels are introduced into the energy-band gap. Affected by factors aforementioned, amorphous semiconductors have special conductive properties, and therefore have great potential in many specific applications.

In the view of the status quo of technology, with the rapid development of microelectronic devices, the first-generation semiconductors (silicon, germanium, etc.) and second-generation semiconductors (gallium arsenide, indium phosphide, etc.) are hard to cater for the requirements for their applications in highly-integration, high-frequency and high-

†Corresponding author. E-mail: liliyang@njupt.edu.cn
‡Corresponding author. E-mail: zengliu@njupt.edu.cn
§Corresponding author. E-mail: whtang@njupt.edu.cn

© 2023 Chinese Physical Society and IOP Publishing Ltd

power microelectronic devices.[9–11] In recent years, the so-called third-generation semiconductors, e.g., silicon carbide (SiC), gallium nitride (GaN), zinc oxide (ZnO), gallium oxide (Ga_2O_3), etc., have come into the centre stage. Compared with the previous two generations of semiconductors, the third-generation semiconductors have a wider bandgap, higher theoretical breakdown electric field strength and higher electron mobility, which are suitable for semiconductor devices operating with high-frequency and high-power, also addressing low power consumption and large density integration.[12–15]

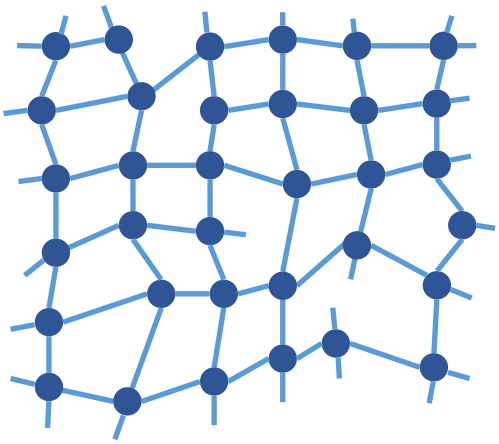


Fig. 1. Schematic structure of amorphous semiconductors.

As a kind of ultra-wide bandgap semiconductor, Ga_2O_3 has a tuneable bandgap of 4.4 eV–5.3 eV via doping and energy-band tailoring,[16,17] possesses excellent physical, chemical and thermal stability, and distinguishes light absorbance in the UV region; therefore it has been extensively studied in recent two decades. Most of the current researches on Ga_2O_3 are focused on crystalline Ga_2O_3, taking advantages of monoclinic β-Ga_2O_3 and orthorhombic ε-Ga_2O_3 among the five crystal structures of Ga_2O_3.[18,19] As shown in Fig. 2(a), the others four phases can be converted into β-phase under some certain conditions, but the mostly-stable β-Ga_2O_3 will not be easily converted to other phases. The β-Ga_2O_3 belongs to monoclinic crystal system with lattice constants of $a = 12.23$ Å, $b = 3.04$ Å, $c = 5.80$ Å, $\alpha = 90°$, $\beta = 103.7°$, $\gamma = 90°$, and space group C_{2h},[20] whose crystal structure is shown in Fig. 2(b) that received the most attention. The bandgap of β-Ga_2O_3 is about 4.4 eV–4.9 eV and the corresponding absorption wavelength is between 253 nm–295 nm; besides, the absorption rate can reach 80% for visible light and UV light, which can be applied to transparent conductive films and deep-UV photoelectric devices.[21,22] In terms of electrical properties, β-Ga_2O_3 has a breakdown electric field strength of 8 MV·cm^{-1} and a Baliga's figure of merit of over 3400, which makes it more suitable for the preparation of power devices relatively than SiC and GaN,[23–25] from the view of theory. However, for crystalline Ga_2O_3, the crystallinity often affects device performance to a great extent, such as the detectivity of photodetectors, thus the preparation process is highly demanded to optimize the crystallinity.

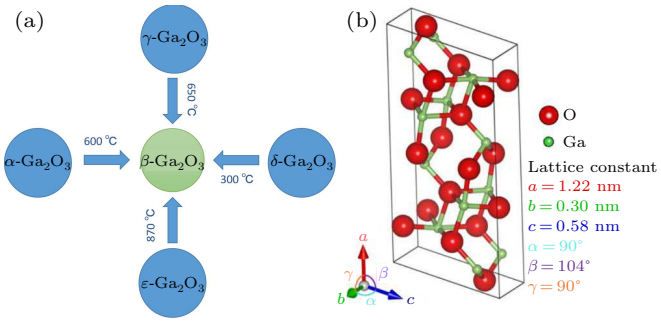


Fig. 2. (a) The conversion relationship of five isomers of Ga_2O_3. (b) Schematic diagram of the crystal structure of β-Ga_2O_3.

In comparison, to date, less research has been done on amorphous Ga_2O_3 (a-Ga_2O_3). Although a-Ga_2O_3 has relatively poor controllability, yet has excellent photoelectric properties; and the preparation process is simpler, with lower requirements for preparation temperature and lower cost, so it is easier to achieve large-area growth.[26,27] In recent years, a-Ga_2O_3 has been proven to have comparable or even better performance especially responsivity and detectivity than single-crystal Ga_2O_3 in the field of deep-UV photodetection.[28] For instance, Wang *et al.*[29] prepared amorphous and β-phase Ga_2O_3 films by magnetron sputtering, and photodetectors were prepared correspondingly, proving that a-Ga_2O_3 PDs had higher responsivity, detectivity and external quantum efficiency, but slower response speed. This is possibly due to the defects trapping and disorders in a-Ga_2O_3. It is well known that flexible devices are often fabricated by using flexible plastic substrates, which typically have a low glass transition temperature of 80 °C–150 °C. However, the high temperature process (at least $\geq$ 400 °C) is essential for the preparation of crystalline Ga_2O_3, which limits the application of crystalline Ga_2O_3 in flexible devices. In contrast, a-Ga_2O_3 prepared at low temperature (even at room temperature) solves this trouble. And, the atoms of a-Ga_2O_3 are arranged disorderly in a long range and orderly in a short range, which allows for better flexibility properties than crystals with ordered structures.[30] Recently, demand for flexible devices has been keeping increasing; therefore, a-Ga_2O_3 is catching more interest from researchers. In addition to these, compared with crystals, there exists a large number of defects inside amorphous materials due to their disordered structure and unsophisticated preparation conditions. In a-Ga_2O_3, oxygen vacancy is a major defect, facilitating a-Ga_2O_3 to have potential applications in RRAMs, gas sensors and some other areas that operate out of oxygen vacancies.

As listed in Fig. 3, this review first summarized main deposition methods of a-Ga_2O_3 thin films, including magnetron sputtering, pulsed laser deposition (PLD), atomic layer deposition (ALD), etc. Device applications of a-Ga_2O_3 thin films

were introduced in the following section, showing the application prospect of a-Ga_2O_3 materials.

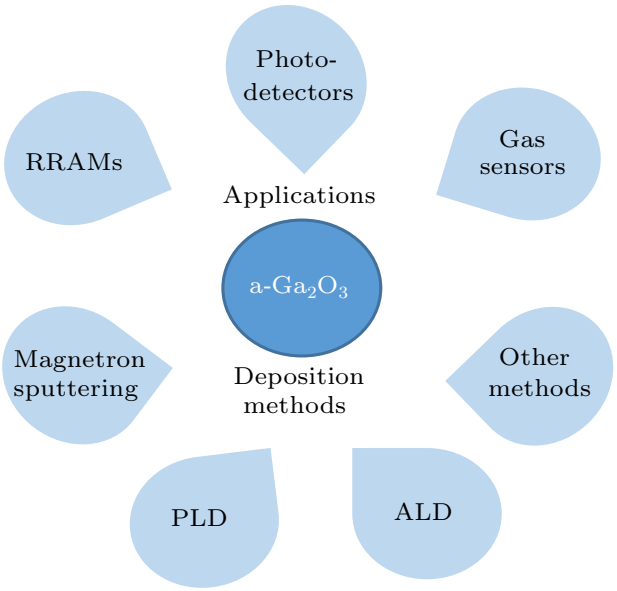


Fig. 3. Main growth methods and applications of a-Ga_2O_3 films.

2. Deposition of a-Ga_2O_3 thin films

There are many methods for the preparation of semiconductor thin films, including physical vapor deposition (PVD) and chemical vapor deposition (CVD); where PVD consists of magnetron sputtering, pulsed laser deposition (PLD), electron beam evaporation, etc., while CVD mainly comprises atomic layer deposition (ALD), Mist-CVD, etc.[18] The a-Ga_2O_3 has low requirements for deposition temperature, and generally transforms into crystals when the growth temperature is higher than about 400 °C,[31,32] so high temperature conditions in the deposition process are almost not required. According to recent studies, the three most used deposition methods of a-Ga_2O_3 thin films are magnetron sputtering, PLD and ALD, as summarized in Table 1. Magnetron sputtering is the most used in the preparation of a-Ga_2O_3, which is simpler to prepare, requires the lowest temperature and has the widest application area. Thin films prepared by PLD and ALD also have some applications. The effects of some experimental factors on film quality for these three along with some other methods are precisely discussed in this section.

Table 1. Summary of properties of a-Ga_2O_3 films deposited by different methods.

Deposition method	Substrate	T_s (°C)	Thickness (nm)	RMS (nm)	E_g (eV)	Application	Refs.
Magnetron sputtering	quartz, PEN	RT	250	–	5.03	solar-blind PDs	[33]
	PEN	RT	250	–	–	flexible x-ray detector	[34]
	sapphire	RT	125		4.9	solar-blind PDs	[35]
	Si (100)	< 500	200	–	–	mechanical performance	[31]
	quartz	RT-500	57.3–93.07	0.794–2.16	4.79–4.96	solar-blind PDs	[36]
	sapphire, glass, PET	RT	90–160	–	~ 3.4	a-CdGaO thin films	[37]
	sapphire	RT	200	1	4.2	IGO solar-blind PDs	[38]
	quartz, PET	RT	250 ± 30	–	–	solar-blind PDs	[39]
	sapphire	RT-300	200	–	~ 5.0	solar-blind PDs	[30]
	Si/SiO_2	RT	–	1.67	4.98	solar-blind PDs for imaging	[40]
	ITO glass	RT	480	–	–	RRAM	[41]
	ITO	–	20	–	–	RRAM	[42]
	$Pt/Ti/SiO_2/Si$	RT	60	–	–	memory device	[43]
	SiO_2/Si	RT	20	–	–	RRAM	[44]
	SiN_x	RT	50	–	–	a-IGZO TFT gas sensor	[45]
	alumina	RT	100	–	–	a-IGZO gas sensor	[46]
	quartz	RT	150	1.10–1.25	–	ozone sensor	[47]
	sapphire	RT	20	~ 5.19	–	a-IGZO ethanol gas sensor	[48]
PLD	$Pt/Ti/SiO_2/Si$	300	200	–	–	RRAM	[49]
	(100) $Nb:SrTiO_3$	500	150	–	–	RRAM	[50]
	quartz	400	200	–	–	dopant activation in a-Ga_2O_3:Sn	[51]
	GZO/alkali-free-glass, quartz	100–425	10, 200	–	4.0–4.5	oxygen deficiency and Sn doping	[52]
	$Cr/SiO_2/Si$	200	10.2–14.5	–	–	RRAM	[53]
ALD	Si/SiO_2	120	200	–	–	dopant activation in a-Ga_2O_3:Sn	[51]
	Si, quartz	200	20.18–40.23	0.77–0.98	4.64–5.25	ZGO films	[54]
	c-Al_2O_3	280	90	–	–	solar-blind PDs	[55]
	alumina with interdigitated Au electrode	150	150	2	–	a-IGZO NO_2 gas sensor	[56]

2.1. Magnetron sputtering

Magnetron sputtering is the most commonly used method to prepare a-Ga_2O_3. Magnetron sputtering makes electrons collide with argon atoms by applying an electric field to ionize them. Argon ions bombard the target with high energy to make the target sputtered, and the sputtered target atoms are deposited on the substrate to form a film.[57,58] Magnetron sputtering has the advantages of fast growth rate, simple process,

strong adhesion and easy for large area sputtering growth, while the uniformity is always an obstacle to overcome.[59]

During magnetron sputtering, the oxygen flux has a certain influence on the quality of the film. In 2017, Cui *et al.* investigated the effect of different oxygen fluxes on the crystallinity of Ga_2O_3 films grown by RF magnetron sputtering at room temperature. The oxygen flux was varied as 0 sccm (pure argon atmosphere), 0.12 sccm, 0.13 sccm, 0.14 sccm, and 0.15 sccm, and corresponding films were labeled as S0, S1, S2, S3, and S4, respectively. The XRD results of the five groups of films showed only the diffraction peaks of amorphous quartz substrates, indicating that Ga_2O_3 film samples are all amorphous. The change of oxygen flux has almost no effect on the transmittance and optical bandgap of Ga_2O_3 films. Then, they fabricate photodetectors based on the five samples, finding that as the oxygen flux increases during film deposition, the dark current and photocurrent of corresponding photodetectors both decrease consequently, which indicates the reduction in oxygen vacancy defects in films.[33] This conclusion is consistent with Liang's research in 2018 and Zhang's research results in 2019,[34,35] which explains that the reduction of oxygen vacancy concentration in the films inhibits the formation of surface traps, leading to the reduction of interface states near the M–S contact, thus inhibiting the sub-bandgap absorption and persistent photoconductivity effects.

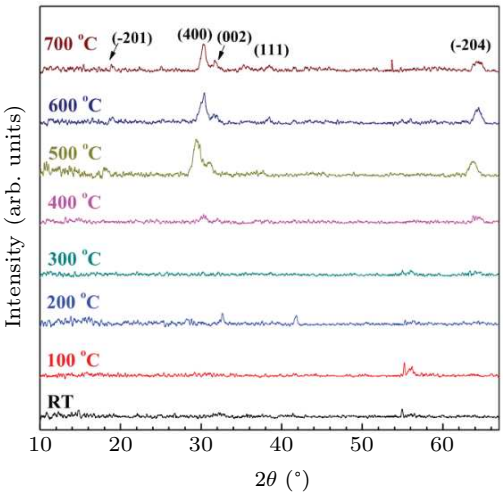


Fig. 4. XRD patterns of a-Ga_2O_3 films. Reproduced with permission from Ref. [31].

In addition to the oxygen flux, the substrate temperature is another essential factor that affects the structure and quality of Ga_2O_3 films. In 2018, Battu and Ramana[31] grew a-Ga_2O_3 films on silicon substrates by magnetron sputtering and investigated the effect of varying substrate temperatures on mechanical properties of Ga_2O_3. The substrate temperature during sputtering is gradually increased from room temperature to 700 °C. As shown in XRD patterns in Fig. 4, when the substrate temperature was at 400 °C and below, the resulting Ga_2O_3 films behave as amorphous, while they stabilize as β-phase nanocrystals after that the substrate temperature reaches 500 °C. Zhu *et al.*[36] investigated the effect of deposition temperature during magnetron sputtering on the performance of a-Ga_2O_3 films and photodetectors, concluding that as the deposition temperature increases, roughness of the film decreases and thickness increases; meanwhile, the concentration of oxygen vacancy in a-Ga_2O_3 increases correspondingly, which results in a higher responsivity.

In addition, for doped films, the gallium content in the film will also affect properties of the film. In 2021, Wang *et al.*[37] prepared $Cd_{1-x}Ga_xO_{1+\delta}$ alloy films on rigid (glass and sapphire) and flexible substrates (PET was used in their work) using RF magnetron sputtering, and the films were amorphous when the Ga content $x > 0.3$. The effects of gallium content on the electrical properties, including carrier concentration, resistivity and mobility of the films, are summarized in Table 2. Moreover, by studying the resistivity changes of $Cd_{1-x}Ga_xO_{1+\delta}$ films under different bending conditions and the scanning electron microscopy images of the film's surface, it is found that the amorphous films with larger gallium content are more resistant to the effects of external forces than that of the crystalline films, and are therefore more suitable for the preparation of flexible devices. Apart from doped Ga_2O_3 thin films, electrode materials can also be selected and doped to improve device properties. Liu *et al.*[60] fabricated a fully transparent a-Ga_2O_3 based photodetector with Al-doped ZnO (AZO) as transparent electrodes by magnetron sputtering, which has excellent performance and is able to clearly detect extremely weak solar-blind UV light signals.

Table 2. Electrical properties of thin films with different gallium content. Reproduced with permission from Ref. [37].

x	N (10^{20} cm^{-3})	Resistivity (10^{-4} Ω·cm)	Mobility μ (cm^2/(V·s))
0.03	5.6	1.46	78.0
0.09	9.0	2.4	29
0.22	4.4	11.4	13
0.38	1.3	20.3	23.5
0.58	0.058	2340	6.25

2.2. Pulsed laser deposition

PLD is a technique that uses laser to bombard a target and deposit the bombarded discharged plasma on the substrate for thin film growth. On the target surface, at a sufficiently high energy density and a sufficiently short pulse time, the target absorbs laser energy and causes the temperature at the spot to rise rapidly above the evaporation temperature of the target, causing the target to evaporate into a regionalized high-temperature, high-density plasma, and under the continued action of the laser beam, the temperature and pressure of the plasma rise rapidly, which then bombards the substrate surface to deposit thin films.[61]

As summarized in Table 1, PLD-grown films are typically used for resistive random access memories (RRAM) due to the

presence of a large number of oxygen vacancies in the film. PLD is often used to grow a-Ga_2O_3 on flexible substrates, and the growth temperature is usually higher than that of magnetron sputtering. In addition, PLD has a slower deposition rate than magnetron sputtering and is therefore not suitable for large area deposition,[62] but it is easier to control the thickness and compactness of the a-Ga_2O_3 thin film.

Multiple reaction sources can be introduced during the PLD growth process, so it can facilitate the doping engineering of a-Ga_2O_3. In 2015, Siah *et al.*[51] used ALD and PLD to deposit Sn-doped a-Ga_2O_3 films on Si/SiO_2 and quartz substrates, respectively. Rutherford backscattering analysis (RBS) was used to measure the stoichiometry of the films grown by ALD and PLD, and the results showed $Ga_2O_{3.41}Sn_{0.065}$ and $Ga_2O_{2.91}Sn_{0.072}$ compound alloys, indicating that the concentration of Sn atoms in the films was 2.3×10^{20} cm^{-3} and 2.9×10^{20} cm^{-3}, respectively. What's more, x-ray absorption spectroscopy (XAS) revealed that the Sn in a-Ga_2O_3 was present in the $+2$ or $+4$ valence charge state depending on the growth conditions.

Worthy to be noted, the substrate temperature is also a significant factor that has an effect on film properties of a-Ga_2O_3. In 2016, Heinemann *et al.*[52] prepared a-Ga_2O_3 thin films by PLD, proposing that there is an effect of deposition temperature on the oxygen vacancy density in the films, which in turn will change the optical bandgap of a-Ga_2O_3 thin films. In their work, several sets of Ga_2O_3 thin film samples were deposited at different temperatures, and the oxygen partial pressure was fixed at 2×10^{-5} mbar for samples setting at 425 °C to 300 °C and 1.3×10^{-3} mbar for samples set at 160 °C to 100 °C. XRD pattern revealed that the grown films all exhibited amorphous states. The relative oxygen content of each a-Ga_2O_3 thin film sample is measured by XPS, and the ratio of O 1s and Ga 2p peak intensity is shown in Fig. 5. The O/Ga ratio tends to 1.5 at high temperature, indicating that the oxygen vacancy concentration in the a-Ga_2O_3 thin film can be effectively reduced by appropriately increasing the growth temperature.

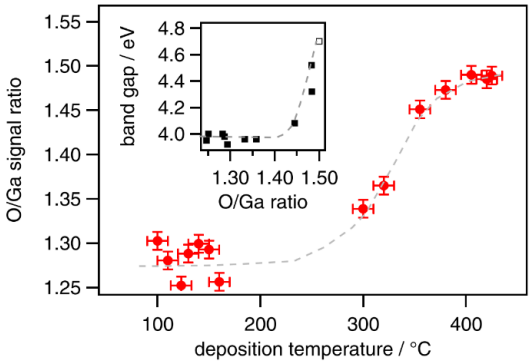


Fig. 5. Ratio of O 1s and Ga 2p peak intensities. The inset shows the correlation between the O/Ga ratio and the optical bandgap. Reproduced with permission from Ref. [52].

2.3. Atomic layer deposition

ALD is another main deposition method of a-Ga_2O_3. Different from magnetron sputtering and PLD, ALD is a chemical vapor deposition method that involves depositing the desired substance layer by layer on the substrate to form a thin film on it. The reaction substances deposited on the atomic level are called as precursors, which contain the elemental components of the desired deposited film. Each precursor forms a separate molecular layer on the surface of the film, so the film can be formed slowly in the intermolecular reaction. ALD can accurately control the thickness of the film with fast and accurate reaction, and has a wide application prospect in the field of precision and high efficiency semiconductor preparation. However, it has the disadvantage of time-consuming and requiring a volatile precursor.[63,64]

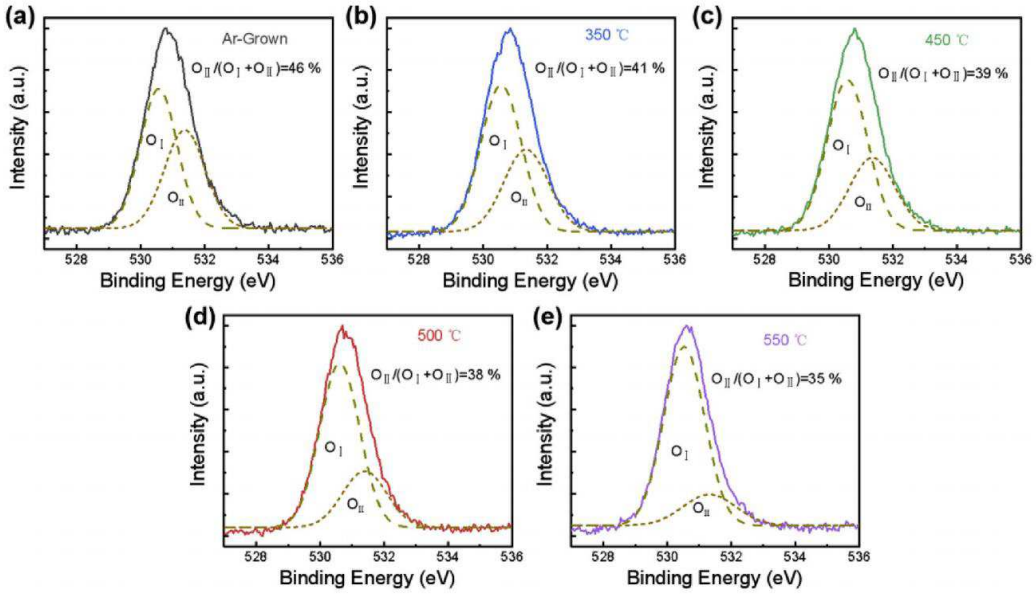


Fig. 6. O 1s XPS spectra of Ga_2O_3 under (a) unannealed, (b) 350 °C annealing, (c) 450 °C annealing, (d) 500 °C annealing and (e) 550 °C annealing. Reproduced with permission from Ref. [55].

As mentioned above, doping can change the properties of a-Ga_2O_3 films to some extent, but doping is often limited by the reaction conditions because different reaction sources have different requirements for the reaction temperature. Tao *et al.*[54] prepared Zn-doped Ga_2O_3 (ZGO) using a combination of plasma-enhanced atomic layer deposition (PE-ALD) of Ga_2O_3 and thermal atomic layer deposition (TH-ALD) of ZnO at a low temperature of 200 °C by superimposing different cycles (7 times, 5 times, and 3 times) of Ga_2O_3 and 1 cycle of ZnO to form sandwich structures. By introducing a combination of different types of ALD techniques, the limitations of reaction conditions for the deposition of doped thin film materials were overcome. The XPS results showed that the oxygen vacancies of ZGO films increased from 27.65% to 37.93%, the band gap increased from 4.64 eV to 5.25 eV, and the surface roughness of the films increased with the increase of Zn concentration.

Furthermore, annealing is an important method to improve the properties of the film. In 2020, Zhou *et al.*[55] prepared solar-blind UV photodetectors based on a-Ga_2O_3 films grown by ALD and investigated the effect of annealing at 350 °C–550 °C in oxygen atmosphere on the detector performance. When the annealing temperature reached 550 °C, the crystallization of β-phase appeared in the films. When the annealing temperature was 500 °C, the 90%–10% decay time of the a-Ga_2O_3 photodetector was decreased to $\sim$ 150 ns, and the UV/visible rejection ratio could be as high as 2.74×10^5, in addition, the dark current at 10 V bias was only 9.43 pA. The O 1s XPS spectra of each sample are shown in Fig. 6, indicating that annealing can effectively reduce the oxygen vacancies in the films.

2.4. Other deposition methods

Mist-CVD method is a new type of material deposition method, which has many advantages such as no need for vacuum condition, low cost and diversified growth sources, which enables it to have great potential for oxide thin film preparation, but there are few studies based on a-Ga_2O_3 thin films deposited by mist-CVD. In 2021, Xu *et al.*[65] grew a-Ga_2O_3 thin films on Si/SiO_2 substrates by mist-CVD for the first time. The growth temperature T_g (300 °C–700 °C) was adjusted in the control experiments to optimize the growth conditions. From the XRD results, it can be seen that the grown samples are amorphous. The XPS results show that the binding energy of O 1s moves to a higher energy level with the increase of T_g, indicating the reduction of oxygen defects in the film. The characteristic peaks of O 1s and Ga 3d of the films grown at 300 °C are weak and irregular, suggesting that low growth temperature is not favorable for the growth of Ga_2O_3 films.

Electron-beam evaporation is a simple thin film deposition method for preparing high purity thin films for optical, electronic, and photoelectric applications, but little research has been done on the deposition of a-Ga_2O_3 films by electron-beam evaporation. In 2020, Li *et al.*[66] prepared a-Ga_2O_3 thin films by electron beam evaporation and investigated the effect of different oxygen partial pressures from 0 Pa to 2.0×10^{-2} Pa on the properties of the films. As shown in Fig. 7, the visible and near-UV transmittance of Ga_2O_3 films improved significantly with increasing oxygen partial pressure, and the optical bandgap increased from 4.3 eV at 0 Pa to 5.1 eV at 2.0×10^{-2} Pa. The trend of laser-induced damage threshold of Ga_2O_3 films with oxygen partial pressure is approximately linearly increasing.

One-pot sputtering refers to a method of preparing materials by dissolving and recrystallizing water as solvent and powder in a sealed pressure reaction vessel. Huang *et al.*[67] prepared three-dimensional a-Ga_2O_3 films on carbon fiber paper (CFP) by one-pot sputtering method and fabricated a new type of solar-blind photoelectrochemical (PEC)-type photodetector based on them. The solid/liquid heterojunction formed a built-in electric field, thus facilitating this PEC-type photodetector to be self-powered.

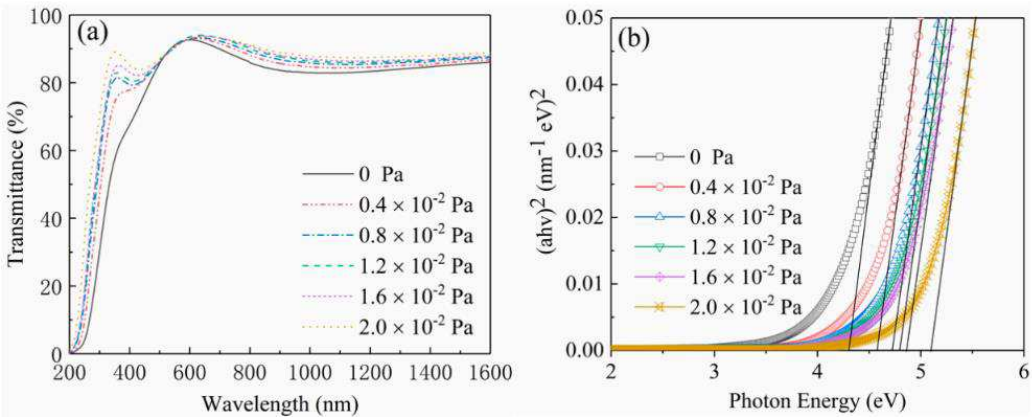


Fig. 7. (a) Optical transmission spectra of a-Ga_2O_3 films deposited at different oxygen partial pressures. (b) Curves of $(\alpha h\nu)^2$ versus $h\nu$. Reproduced with permission from Ref. [66].

3. Device applications of amorphous Ga_2O_3 thin films

Currently, a-Ga_2O_3 has meaningful applications in many fields. a-Ga_2O_3 has good photoelectric properties and is widely used in deep-UV solar-blind detectors, solar cells, etc. Since there are often a large number of oxygen vacancies in a-Ga_2O_3, the resistive switching mechanism dominated by oxygen vacancies is remarkable, which enables it to be applied to RRAMs. Under certain conditions, the resistivity of a-Ga_2O_3 changes with the concentration of redox gases such as oxygen and ozone, and therefore a-Ga_2O_3 has applications in gas sensors. In addition, the long-range disorder and short-range order characteristics of a-Ga_2O_3 make it have good mechanical properties and can be used to prepare flexible devices. In this section, we focus on the frontiers of a-Ga_2O_3 applications.

3.1. Photodetectors

As shown in Fig. 8(a), photodetectors are devices that convert optical radiation to electrical signals through the photoelectric effect of materials to achieve information transmission, and have important applications in many civil and military fields. The operation of photodetectors is generally based on photoconductive effect and/or photovoltaic effect. The structure of photodetectors based on photoconductive effect is usually metal–semiconductor–metal (MSM). Generally, the electrons in the valence band of semiconductors will not automatically jump into the conduction band because there is a band gap (E_g) between the conduction band and the valence band. Under illumination, after absorbing the photon energy of a certain wavelength ($E \geq E_g$), electrons in the valence band of the semiconductor will jump into the conduction band, resulting in photogenerated electron–hole pairs (excitons). At this time, electrons do not escape from the surface of the material, which will lead to an increased conductivity and thereupon a decreased resistance. The structure of photodetectors based on photovoltaic effect includes Schottky junction, heterojunction, etc. Photovoltaic effect refers to the effect that the separation and migration of photogenerated carriers in the space charge region of the junction will cause the generation of photogenerated electromotive force after the semiconductor material absorbs the photon energy. When the junction absorbs the photon energy (for a certain wavelength), the photogenerated electron–hole pairs will be excited. Driven by the built-in electric field, the photogenerated carriers are rapidly separated, and eventually a large number of holes are accumulated on one side, and electrons are accumulated on the other side, so the photogenerated electromotive force is formed owing to the construction of the junction. If the two poles are connected to the load resistance, there will be photogenerated current passing through in the current loop of the photodetector.

Ga_2O_3 is an ultra-wide bandgap semiconductor material with a bandgap of 4.4 eV–5.3 eV, and its corresponding absorption region is exactly in the solar-blind deep UV region. The simple fabrication process of a-Ga_2O_3, along with its good photoelectric properties, makes it an ideal material for application in deep-UV photodetectors. Due to lots of defects and impurities in a-Ga_2O_3, in addition to the above intrinsic transitions, there will also be extrinsic transitions caused by defect and impurity levels in the band gap. As shown in Fig. 8(b), the existence of impurity and defect energy levels will enable Ga_2O_3 to absorb long-wavelength photons whose energy is smaller than the band gap, resulting in extra carrier migration and sub-band absorbance. In addition, the energy levels in the band gap will be the recombination centers of non-equilibrium carriers, and may be traps to capture them. When a non-equilibrium minority carrier is trapped, there will be a non-equilibrium majority carrier that maintains electrical neutralization with it, resulting in additional conductivity. The existence of traps makes the non-equilibrium carriers unable to rapidly recombine and decay when the light is turned off, thus increasing the relaxation time from the non-equilibrium state to the equilibrium state. Based on the above factors, a-Ga_2O_3 based photodetectors usually have higher responsivity but longer response time. Moreover, in recent years, the demand for wearable devices in a variety of fields has been increasing dramatically, leading to the rapid development of flexible devices, also in the field of UV detection. a-Ga_2O_3 has been used in many flexible UV photodetectors due to its unique amorphous structure and low preparation temperature.

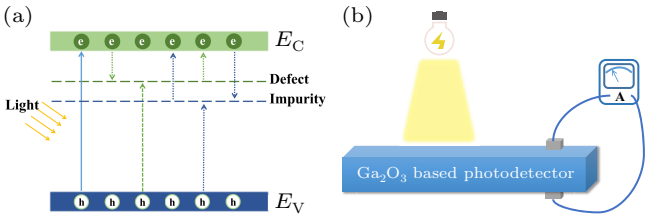


Fig. 8. (a) Basic operation mechanism of Ga_2O_3 based photodetectors. (b) The energy-band of a-Ga_2O_3 based photodetectors.

As mentioned above, factors such as oxygen flux, substrate temperature, and annealing may well affect the detector performance from the view of materials characterizations. Taking oxygen flux as an example, Liang *et al.*[34] prepared x-ray photodetectors based on the a-Ga_2O_3 films, and five samples D1–D5 were experimentally set up, corresponding to oxygen fluxes of 1.6×10^{-3} Pa, 1.4×10^{-3} Pa, 1.2×10^{-3} Pa, 1.0×10^{-3} Pa, and 0 Pa. The oxygen vacancies in the films decreased with the increase of oxygen fluxes during the sputtering process. Figure 9(a) shows the time-dependent photocurrents of D1–D5 at 10 V bias when the x-ray source is switched on and off, and the results show that the samples have good de-

tection performance for x-rays, but the increase of oxygen vacancies leads to more severe persistent photoconductivity effects in the detector. In addition, the possibility of a-Ga_2O_3 in the fabrication of flexible x-ray detectors is also discovered by bending and fatigue tests, and the results are depicted in Figs. 9(b)–9(d).

Photodetectors can be divided into a variety of structures, and different structures can affect the detection performance.

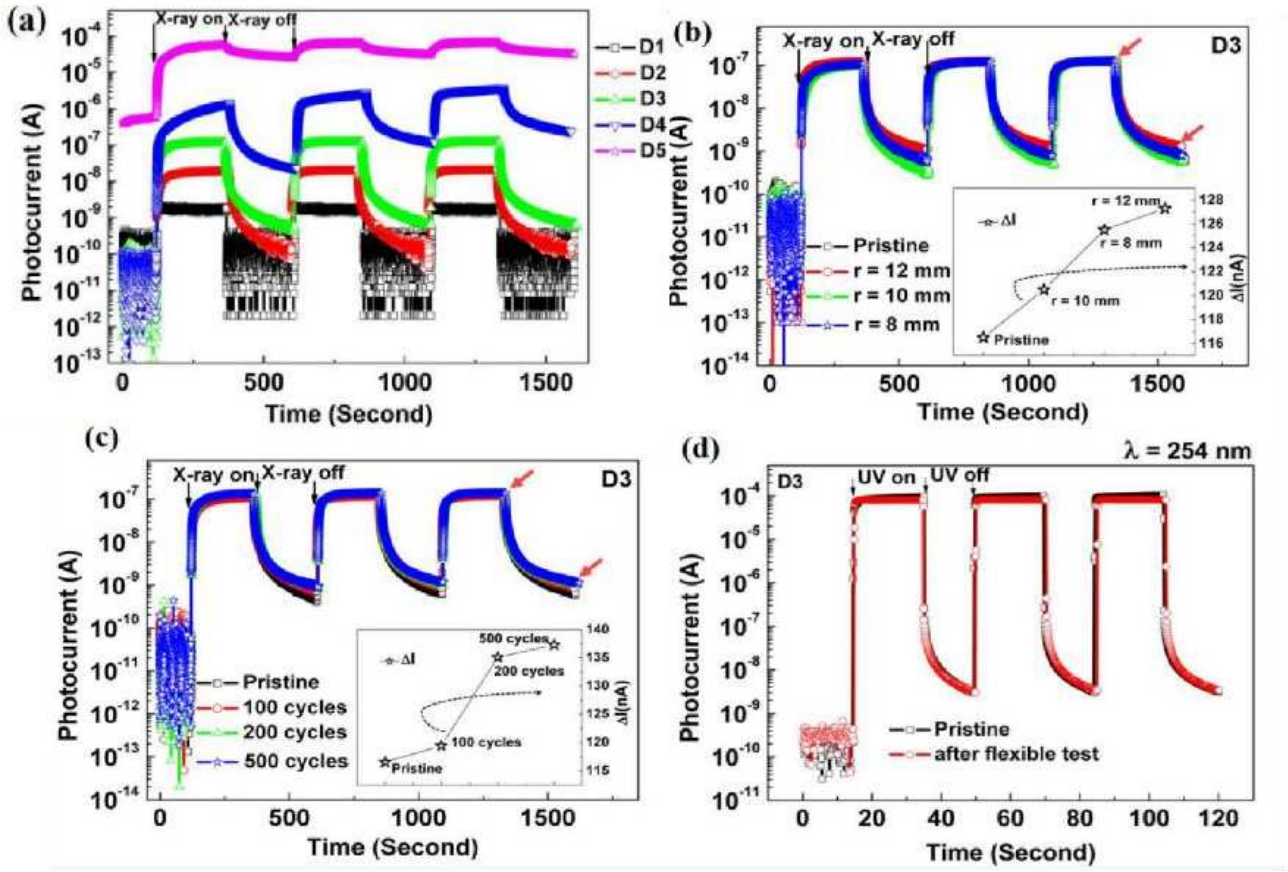


Fig. 9. (a) Time-dependent photocurrent of D1–D5 at 10 V bias. (b) Photoresponse performance of D3 exposed to x-rays under plane and different bending radius as a function of time. (c) Time-dependent photoresponse of D3 exposed to x-rays after 0 bends, 100 bends, 200 bends, and 500 bends with $r = 8$ mm. (d) Time-dependent photoresponse of D3 exposed to 254 nm light after all flexibility tests. Reproduced with permission from Ref. [34].

Table 3. Summarizes some main parameters of various photodetectors in recent studies.

Structures	Materials	R (A·W^{-1})	EQE (%)	D^* (Jones)	Rise/decay time (μs)	PDCR	Reference
MSM	a-Ga_2O_3	0.19	–	–	–/19.10	$> 10^4$	[33]
3D MSM array	a-Ga_2O_3	8.9	4450	3.3×10^{13}	–/308	$> 10^3$	[68]
MSM	a-IGO	18.06	–	–	4.9/230	–	[38]
MSM	a-IZO/a-Ga_2O_3	43.99	2.18×10^4	–	$6.14 \times 10^6/2.32 \times 10^6$	10^2	[39]
Phase junction	amorphous/crystalline Ga_2O_3	0.81	400	5×10^{14}	$12 \times 10^{-3}/19.6$	1.2×10^7	[30]
MSM	a-Ga_2O_3	6.54×10^{-2}	–	9.82×10^{12}	–/243.9	10^5	[35]
MSM	a-Ga_2O_3	1099	–	–	–	–	[69]
TFT	a-Ga_2O_3	5.67×10^3	–	1.87×10^{15}	$-/5 \times 10^3$	5×10^7	[70]
Heterojunction	graphene/a-Ga_2O_3	22.75	1.1×10^4	8.2×10^{13}	–	$\sim 10^5$	[71]
MSM	a-Ga_2O_3	138	–	$\sim 1.1 \times 10^{14}$	$5.2 \times 10^5/3.2 \times 10^5$	2258	[36]
MSM	a-Ga_2O_3	733	4.1×10^5	3.9×10^{16}	$1 \times 10^3/18 \times 10^3$	3.9×10^7	[40]
Heterojunction	polycrystalline $CH_3NH_3PbCl_3$/a-Ga_2O_3	4.96×10^{-3}	–	5.4×10^{10}	$5.6 \times 10^4/6.7 \times 10^4$	890	[72]
MSM	nano-Ag/a-Ga_2O_3	0.014	6.83	2.04×10^{13}	$4.97 \times 10^5/2.22 \times 10^5$	3.15×10^6	[73]

3.1.1. Metal–semiconductor–metal structured photodetectors

Metal–semiconductor–metal (MSM) structured photodetectors are most widely used due to their simple fabrication process and low production cost. In 1979, Sugeta *et al.* improved on the conventional photodiode by proposing a MSM structure, which forms a pair of centrally symmetrical crossed finger electrodes on the semiconductor surface, with the area between the pair of electrodes serving as the illuminated area, thereby the effective illuminated area is expanded.

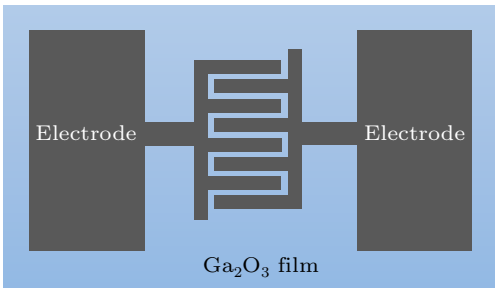


Fig. 10. Schematic diagram of MSM structured photodetector.

In 2019, Fang *et al.*[38] prepared a high-performance MSM solar-blind UV photodetector based on an In-doped a-Ga_2O_3 film (a-IGO). As illustrated in Fig. 11(a), the detector responded up to 18.06 A/W at 235 nm with a rise time of 4.9 μs and a decay time of 230 μs, and the detection range was extended from 210 nm to 330 nm due to the doping that changed the band gap of the film. This phenomenon can be interpreted by the function of impurity energy level. With the introduction of the impurity energy level, Ga_2O_3 can absorb photons with lower energy, thus the detection range could be extended. In addition to the above methods for adjusting the preparation conditions, there are some other methods to improve the performance of photodetectors. In 2019, Zhou *et al.*[69] reported a high-gain UV-VIS-NIR photodetector based on an a-Ga_2O_3 film. The device exhibits ultra-high photovoltaic performance, and the thermal excitation accelerates electron–oxygen vacancy complexation through a novel thermal relaxation (TR) process that can effectively reduce the dark current and reduce the device recovery time from hours to seconds without affecting the gain of the device.

Due to the high intensity of internal defects, a-Ga_2O_3-based photodetectors generally have high dark current. In order to solve this problem without sacrificing the photocurrent, Yang *et al.*[73] fabricated a novel nano-Ag/a-Ga_2O_3-based MSM photodetector with superior responsivity and ultra-low dark current of 14.7 fA at 5 V. Through simple room-temperature magnetron sputtering technology and subsequent 200 °C annealing process, sporadic Ag nanostructures were introduced to form scattered local Schottky junctions at the interface between In electrode and a-Ga_2O_3 film. The excellent photodetector performance suggested that the introduction of local Schottky junctions is a promising method to optimize the performance of amorphous semiconductor-based photodetectors.

The application of conventional metal electrodes on flexible photodetectors is limited because they are not foldable, so it is necessary to find an electrode material suitable for flexible devices. In 2019, Kumar *et al.*[39] prepared solar-blind UV photodetectors based on the a-Ga_2O_3 thin films using amorphous indium zinc oxide (a-IZO) as a transparent conducting electrode instead of conventional metal electrodes. The optical responsivity of the detector was 48.99 $A{\cdot}W^{-1}$ and the external quantum efficiency was 2.18×10^4%, while the optical responsivity and EQE of the conventional metallic electrode were only 0.12 $A{\cdot}W^{-1}$ and 60%. In addition, after bending fatigue test shown in Fig. 11(b), the photocurrent of the device only decreased by 38.8% after 500 stretch-release cycles, while the conventional metal electrode failed at a single bend with a radius of 30 cm, indicating that the solar-blind UV photodetector based on a-Ga_2O_3 film and a-IZO transparent conducting electrode could be applied in flexible solar-blind photodetectors.

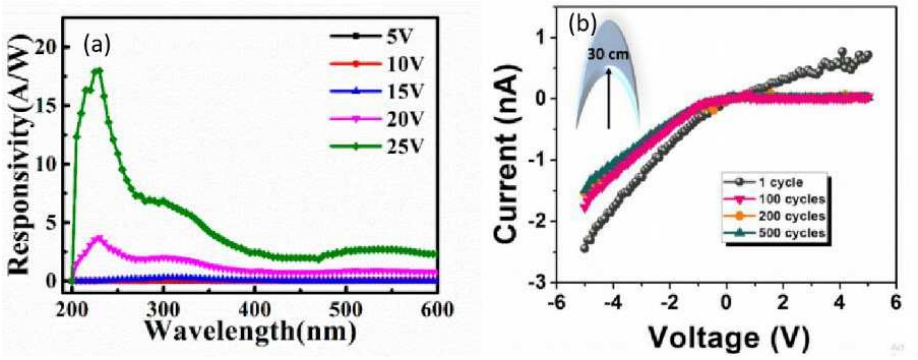


Fig. 11. (a) Response spectrum of a-IGO photodetector. Reproduced with permission from Ref. [38]. (b) *I*–*V* curves of a-Ga_2O_3 photodetector based on a-IZO electrode under 254 nm DUV illumination after bending radius $r = 30$ cm and bending periods of 1, 100, 200, and 500. Reproduced with permission from Ref. [39].

In addition to simple photodetection, there are currently many studies on MSM structured photodetector arrays for imaging. It is well known that photodetectors can be used for imaging by capturing light sources. The imaging system that uses a single detector to image by moving the light source is complex and inefficient, while the array imaging system with multiple detectors highly integrated can solve the above problems. In 2021, Qin *et al.*[40] prepared a high-performance MSM-type solar-blind UV detector based on annealed a-Ga_2O_3 films, which exhibited an ultra-high responsivity of 733 $A{\cdot}W^{-1}$, a high response rate of 18 ms, and a light-to-dark current ratio of 3.9×10^7. In addition, a 32×32 image sensor array based on post-annealed a-Ga_2O_3 solar-blind photodetector was prepared, as schematically shown in Fig. 12,

and this image sensor array presented excellent optical pattern recognition. Chen *et al.*[68] prepared a 3D photodetector array, which achieves an extremely wide detection space angle and good spatial recognition capability that cannot be achieved by two-dimensional photodetectors. The three-dimensional solar-blind photodetector array is based on the a-Ga_2O_3 films grown on PET substrates, with a dark current of only 0.17 nA, a peak response of 8.9 A·W^{-1} at 250 nm, an external quantum efficiency of more than 4450%, a UV/visible rejection ratio of 10^3, a solar-blind ratio of 10^2, and a cut-off wavelength of 268 nm. In the bending fatigue test, the device exhibits excellent electrical stability even after thousands of bends. All photoelectric properties mentioned above are depicted in Fig. 13. Surprisingly, the three-dimensional solar-blind detector also realizes the detection of real time trajectory and multi-point light spatial distribution.

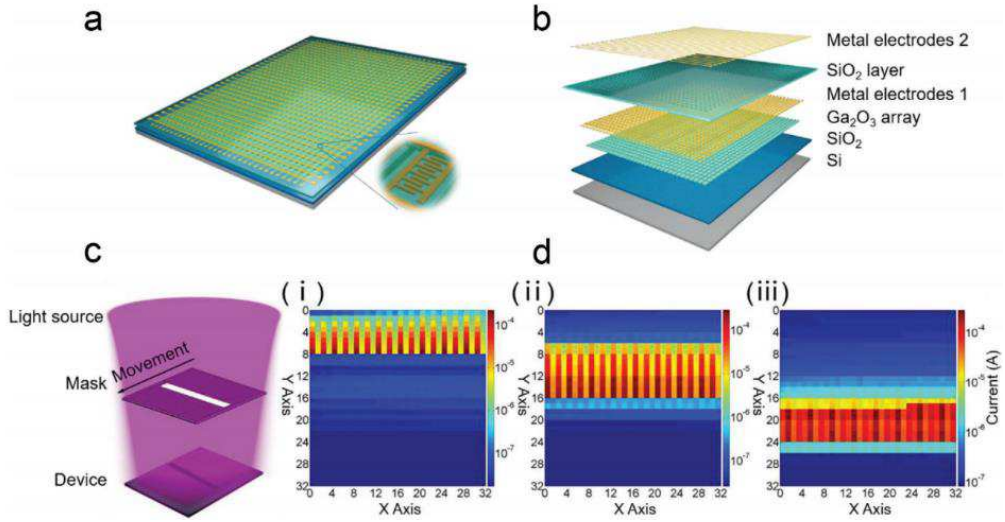


Fig. 12. (a) Schematic diagram of a 32×32 a-Ga_2O_3 image sensor. (b) Schematic of the decomposition of the image sensor. (c) Schematic of the imaging operation for beam motion measurement. (d) Demonstration of the output image at different positions during motion. Reproduced with permission from Ref. [40].

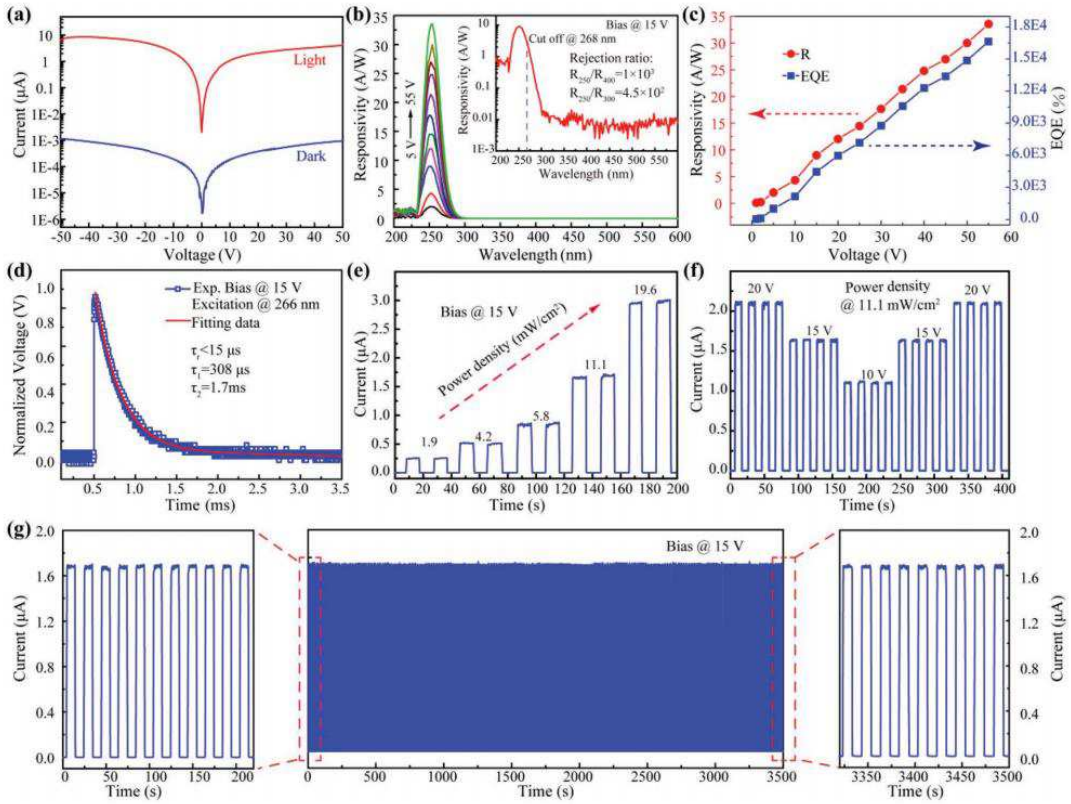


Fig. 13. (a) *I*–*V* characteristics of the photodetector cell under 150 W xenon lamp illumination. (b) Response spectrum of the Ga_2O_3 photodetector cell. (c) Dependence of the maximum responsivity and EQE of the photodetector cell on the applied bias. (d) Normalized transient photoresponse characteristics were measured at 15 V bias with 266 nm pulsed laser excitation. *I*–*t* curves for different (e) light irradiation powers and (f) bias voltages. (g) Dynamic response of the photodetector under switching modulated light over a test period of 170 cycles. Reproduced with permission from Ref. [68].

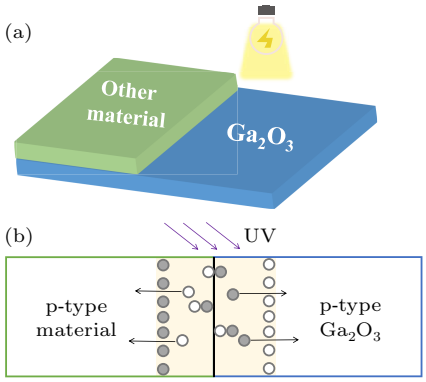


Fig. 14. (a) Schematic diagram and (b) operation mechanism of heterojunction structured photodetector.

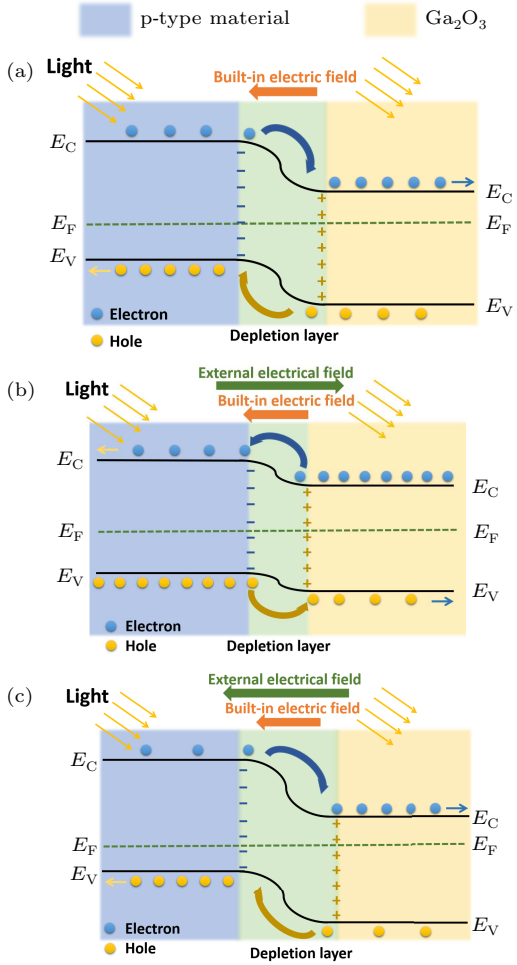


Fig. 15. The energy band diagrams of heterojunction structured photodetector at (a) 0 bias, (b) forward bias, and (c) reverse bias.

3.1.2. Heterojunction structured photodetectors

Self-powered photodetectors that can work without external bias and multi-band UV photodetectors with multi-band detection are promising for many future commercial and military applications, and these functions can be achieved by constructing heterojunctions. Due to the difference in charge concentration and energy band alignment of the two materials, a built-in electric field will be formed at the interface owing to charge migration after contact, and the electron–hole pairs excited by light can be separated by the built-in electric field, and drift without an applied voltage, thus realizing self-power.

In 2020, Wang *et al.*[71] prepared a flexible solar-blind photodetector based on a graphene/a-Ga_2O_3 van der Waals heterojunction with a light-to-dark current ratio of 10^5, a responsivity of 22.75 A·W^{-1} at 254 nm UV illumination, and EQE and responsivity of 1.1×10^4% and 8.4×10^{13} Jones, respectively. In addition, the device exhibited excellent flexibility, with performance remaining almost unchanged after several bending and torsion experiments. In 2022, Liu *et al.*[72] prepared a high-performance, self-powered UVA photodetector based on a polycrystalline $MAPbCl_3$/a-Ga_2O_3 heterojunction, which is schematically shown in Fig. 16(a). The photoelectric properties are illustrated in Figs. 16(b)–16(e), compared with the polycrystalline $MAPbCl_3$ device, the responsivity of the polycrystalline $MAPbCl_3$/a-Ga_2O_3 heterojunction at zero bias increased from 7.36×10^{-2} mA·W^{-1} to 4.96 mA·W^{-1}, the rise time shortened from 4.327 s to 56 ms, the decay time shortened from 3.211 s to 67 ms, and the light-to-dark current ratio increased from 2 to 890. In addition, the detector has a detection of up to 5.4×10^{10} Jones without external bias, which demonstrates excellent self-powered performance. On the other side, the preparation of heterojunctions can easily introduce lattice mismatches that lead to the formation of defects and dislocations at the interface, compromising device performance and limiting its applications. In 2019, Wang *et al.*[30] prepared a high-performance solar-blind photodetector based on an amorphous/crystalline Ga_2O_3 phase junction by magnetron sputtering, which avoided the effects of lattice mismatch. The heterojunction photodetector possesses a response rate of 0.81 A·W^{-1}, a detection rate higher than 5.67×10^{14} Jones, an ultra-fast response rate ($\sim$ 12 ns/19.6 µs for rise/decay time), and a PDCR of more than 10^7. The excellent photoelectric performance of the device is due to the amorphous/crystalline interfacial field that promotes the separation of electron–hole pairs.

3.1.3. Thin-film transistor structured photodetectors

Unlike the above two structures, thin-film transistors are three-terminal devices that can control channel carrier transport through the gate, thereby suppressing persistent photoconductivity (PPC) and achieving both high responsivity and high speed of response. In 2020, Han *et al.*[70] prepared bottom-gate a-Ga_2O_3 thin-film transistors (TFTs) with a three-terminal TFT structure that allows the photodetector to achieve a balance of high responsivity and fast response rate, and used a novel tetramethylammonium hydroxide (TMAH) solution as an etching solution during device fabrication, schematic structure and photoelectric properties of which are displayed in Fig. 17. Under 254 nm UV illumination, the a-Ga_2O_3 phototransistor has a photo-to-dark current ratio of 5×10^7, a response rate of 5.67×10^3 A·W^{-1}, and a detection rate of 1.87×10^{15} Jones.

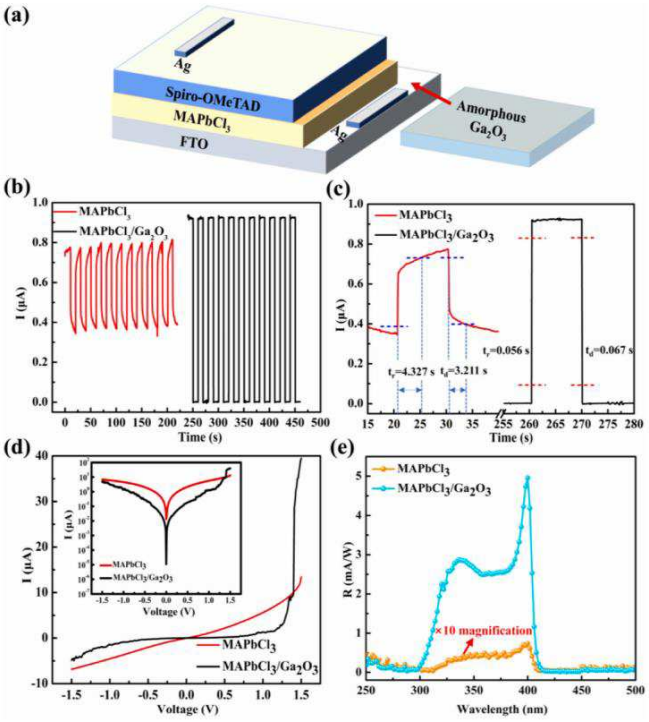


Fig. 16. (a) Schematic of the device structure was improved by inserting an a-Ga_2O_3 layer. (b) *I*–*t* curves of $MAPbCl_3$ devices and $MAPbCl_3$/a-Ga_2O_3 devices. (c) Rise and decay times of $MAPbCl_3$ devices and $MAPbCl_3$/a-Ga_2O_3 devices in a single switching cycle. (d) $MAPbCl_3$ devices and $MAPbCl_3$/a-Ga_2O_3 devices with dark *I*–*V* curves. (e) Responsivity of $MAPbCl_3$ devices and $MAPbCl_3$/a-Ga_2O_3 devices. Reproduced with permission from Ref. [72].

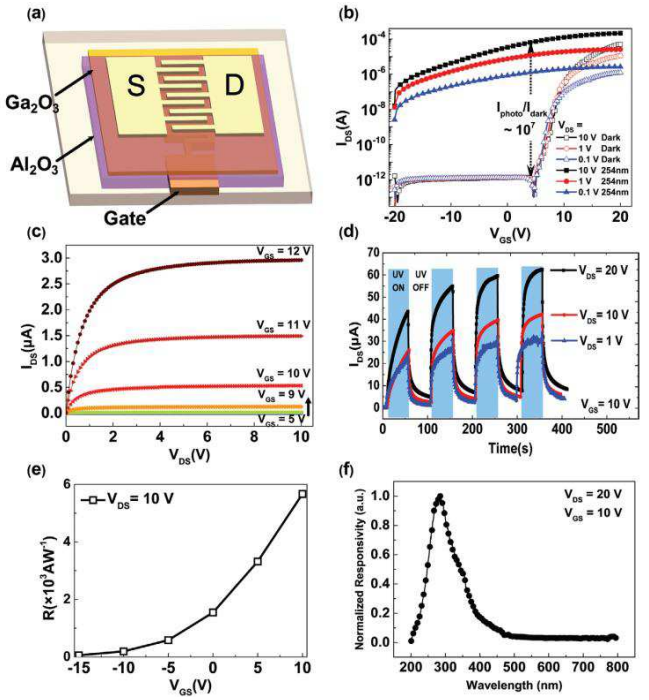


Fig. 17. (a) Schematic structure of a-Ga_2O_3 phototransistor on quartz. (b) I_{DS}–V_{GS} curves were recorded under dark and 254 nm UV irradiation (45 μW·cm^{-2}) for different V_{DS}. (c) I_{DS}–V_{DS} curves were recorded at different V_G. (d) I_{DS}–V_{DS} curves under 254 nm UV irradiation (45 μW·cm^{-2}) at different V_{DS}. (e) Time-dependent photoresponse curves were measured under 254 nm UV illumination (45 μW·cm^{-2}) at different V_{GS}. (f) Normalized photoresponse spectra of PD at V_{DS} of 20 V and V_{GS} of 10 V. Reproduced with permission from Ref. [70].

3.2. Resistive random access memory

RRAM, as a new generation of memory devices, is attracting more and more attention from researchers because of its simple structure (MIM sandwich structure), low operating voltage and easy integration. Amorphous Ga_2O_3 is a wide bandgap semiconductor with high resistive properties and a large number of oxygen vacancies, making it an ideal material for resistive random access memories. The resistive mechanism of RRAM is very complex, but there is no uniform conclusion on the resistive conversion mechanism of RRAM, and a single resistive behavior may be formed by a combination of mechanisms. However, researchers generally believe that the diffusion of oxygen vacancies plays an important role. In 2019, Yang *et al.*[42] prepared a-Ga_2O_3 based RRAM devices by RF magnetron sputtering, varied the oxygen flux during the film preparation to adjust the oxygen vacancies in the films, and explored the oxygen fluxes that enable the devices to have optimal performance. The results show that the device samples exhibit excellent electrical performance with a maximum cycle number of 220, I_{on}/I_{off} of 5×10^4, and retention time of 10^4 s at a reading voltage of 0.1 V and an oxygen concentration of 25%, with optimal repeatability and retention.

According to previous studies, the resistive transition mechanism of RRAM can be mainly classified into: conducting filament model (CF), Poole–Frenkel emission, Schottky emission, and space charge-limited current effect (SCLC).[74] The following summarizes some of the research on a-Ga_2O_3-based RRAMs and the researchers' explanations of their mechanisms.

Currently, the operating mechanism of RRAM based on space charge confinement current has been widely accepted, where free carriers are injected from an electrode into the conduction band of a solid dielectric, causing a conduction current in the dielectric. When the density of these injected additional carriers exceeds the intrinsic thermal equilibrium carrier density, the current will be limited only by the space charge formed by the injected carriers themselves, forming the so-called space charge limited current. The other most common mechanism is conductive filament. The specific mechanism of operation is the introduction of metal ions in active electrodes by an applied voltage, forming conductive pathways similar to conductive filaments, which may be composed of metal ions or vacancy defects, etc. In many cases, these two mechanisms occur simultaneously.

In 2015, Guo *et al.*[49] explored the resistive switching performance of Pt/Ga_2O_{3-x}/Pt structures by depositing a-Ga_2O_3 films with heavy oxygen vacancies on Pt/Ti/SiO_2/Si substrates using laser pulses. The resistive behavior is unipolar, with an off/on resistance ratio as high as 10^4, a non-overlapping switching voltage, and good repeatability and retention. In addition, based on the *I*–*V* relationship curve of

the switching state and the temperature dependence of the resistance (Figs. 18(a) and 18(b)), it is shown that the resistive switching mechanism is caused by the formation and rupture of resistive filaments formed by oxygen vacancies. In 2019, Zhang *et al.*[43] investigated the resistive switching phenomenon of Ti/Ga_2O_3/Pt memory devices in the dark and UV illumination states. The typical unipolar RS behaviors are presented in Figs. 18(c) and 18(d). It is proposed that UV light can induce photogenerated carriers and oxygen defects, which will lower the Schottky barrier and facilitate the formation of conducting filaments under the electric field, reducing their formation and switching voltage. The photogenerated oxygen defects can form multiple conducting filaments under the electric field, thus achieving multilevel memory. In 2020, Li *et al.*[53] prepared RRAM based on a-Ga_2O_3/ZnO composite film by ALD, and controlled the concentration of Zn by adjusting the number of Ga_2O_3/ZnO deposition cycles in the ALD process. It was demonstrated that the introduction of Zn in the Ga_2O_3 film could introduce more oxygen vacancies, thus controlling the concentration of oxygen vacancies and promoting the formation of conductive filaments in the film. The experiments showed that when the Zn content is at 31%, the RRAM device exhibited excellent performance with an HRS/LRS of about 10^3, a retention time of more than 10^4 s, and stable 100 cycles.

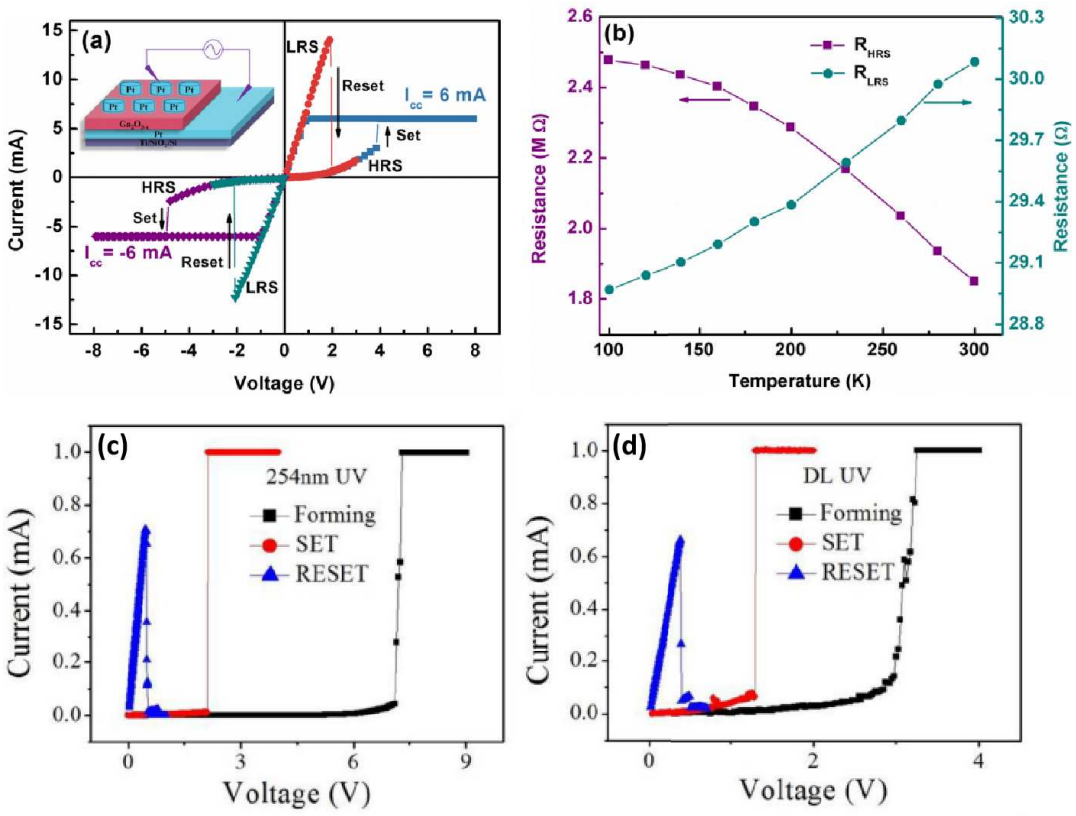


Fig. 18. (a) The *I*–*V* relationship curve and (b) temperature dependence of resistance of Pt/Ga_2O_{3-x}/Pt monopole switch. Reproduced with permission from Ref. [49]. Formation and monopole RS process of Ti/Ga_2O_3/Pt memory devices under (c) 254 nm UV and (d) DL UV irradiation. Reproduced with permission from Ref. [43].

Table 4. Summary of main parameters and resistive mechanism of RRAMs with various structures.

Structures	Mechanism	Switching behavior	Retention time (s)	Max cycles	HRS/LRS	Reference
Pt/Ga_2O_{3-x}/Pt	SCLC and CF	unipolar switching	10^4	70	10^4	[49]
Au/Ga_2O_{3-x}/Nb:$SrTiO_3$/Au	SCLC	bipolar switching	10^3	50	10^3	[50]
Cu_2O/Ga_2O_3	SCLC and Poole–Frenkel emission	both unipolar and bipolar switching	10^4	–	10^2	[41]
Al/Ga_2O_3 /ITO	SCLC and CF	bipolar switching	10^4	220	7×10^5	[42]
Ti/Ga_2O_3/Pt	SCLC and CF	unipolar switching	–	–	10^2	[43]
Ga_2O_3/ZnO	SCLC and CF	unipolar switching	10^4	100	6×10^3	[53]
Ta/Ga_2O_3/Pt	SCLC	bipolar switching	10^4	3×10^6	40	[44]

In 2015, Wang, Li *et al.*[50] used laser pulse deposition technique to grow Au/Ga_2O_{3-x}/Nb:$SrTiO_3$/Au heterostructures of a-Ga_2O_3 films on Nb-doped $SrTiO_3$ substrates and found that the devices have differential negative resistance (NDR) and bipolar resistive switching (RS) phenomena (Fig. 19), the principle of which can be explained

by SCLC, i.e., changes in the space charge region at the Ga_2O_{3-x}/NSTO interface and the capture and release of electrons by the interfacial state, where the rate of electron release depends on the magnitude of the applied voltage, thus leading to the NDR phenomenon. In 2020, Yang *et al.*[44] prepared Ta/Ga_2O_3/Pt structured RRAM devices, which exhibited good resistive switching performance with a high resistance ratio of HRS/LRS, up to 3×10^6 switching cycles, and good switching coherence with SCLC effect. By integrating PZT piezoelectric ceramics with RRAM, a reliable self-powered system was developed to recognize sudden pressure modulation and store the information as LRS or HRS of the RRAM device.

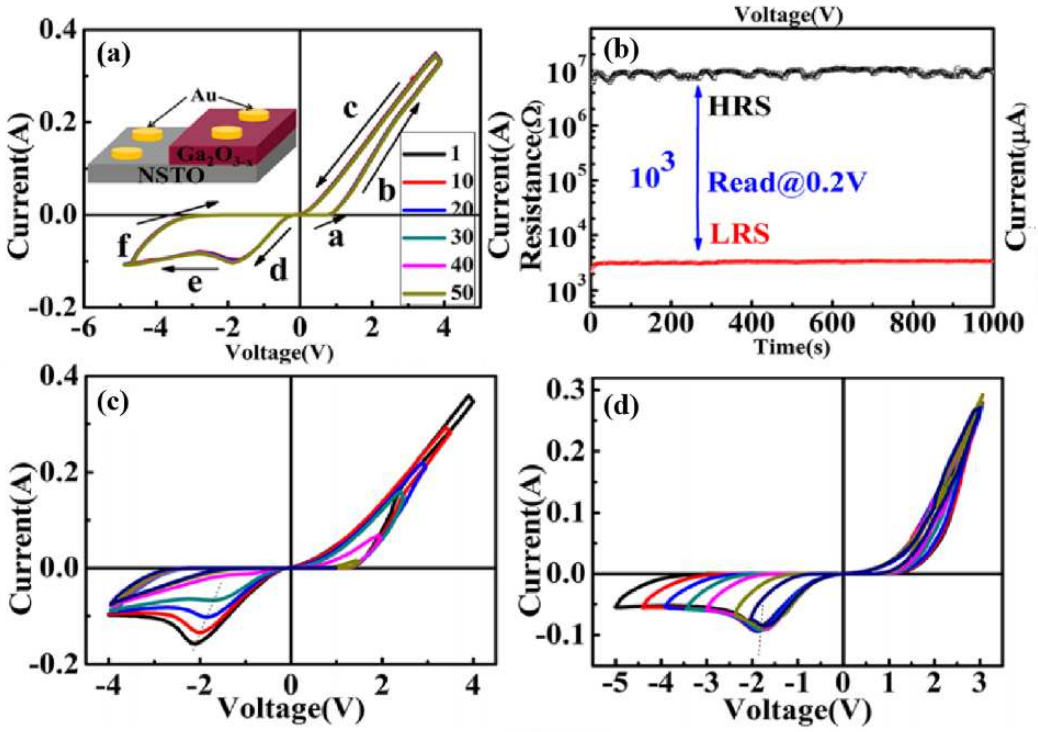


Fig. 19. (a) Typical *I*–*V* characteristics and (b) time retention characteristics of HRS and LRS after placement and reset of Au/Ga_2O_{3-x}/NSTO/Au devices. *I*–*V* curves of Au/Ga_2O_{3-x}/NSTO/Au structure with increasing (c) positive voltage while keeping the maximum negative voltage at −4 V and (d) negative voltage while keeping the maximum positive voltage at 2.5 V. Reproduced with permission from Ref. [50].

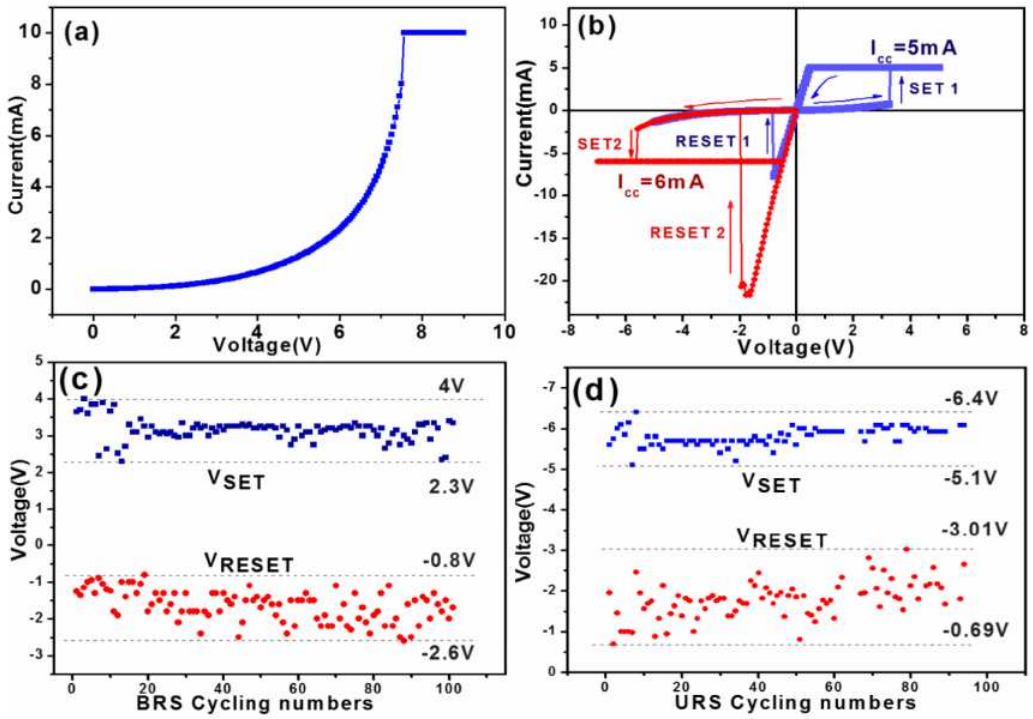


Fig. 20. (a) Electrical formation process of RRAM devices. (b) *I*–*V* curves in BRS (blue curve) and URS (red curve) modes. (c) V_{SET} and V_{RESET} in BRS mode. (d) V_{SET} and V_{RESET} in URS mode. Reproduced with permission from Ref. [41].

The Poole–Frankford emission mechanism is an emission mechanism associated with traps, where the charge in the trap is excited to the conduction band of the insulator when a voltage is applied to the device, which basically works by allowing the Coulomb potential to confine the state of the electrons. It is a volume-constrained conduction mechanism. In 2016, Zhi and Li *et al.*[41] prepared a-Ga_2O_3/CuO structured RRAM devices by magnetron sputtering and observed the existence of unipolar resistive switching (URS) and bipolar resistive switching (BRS) phenomena in the devices, with controlled and reversible transitions between URS and BRS (Fig. 20), which can be explained by a combination of SCLC and Poole–Frenkel emission.

Schottky emission mechanism is that the oxygen vacancies at the interface between the substrate and the electrode can trap and release charge, resulting in a corresponding change in the interfacial Schottky barrier, which causes the device resistance to shift between high and low resistance states. There are relatively few studies on the mechanism in a-Ga_2O_3-based RRAMs.

3.3. Gas sensors

Gas sensor is a kind of sensor equipment that converts information such as certain gas concentration in the environment into electrical signals. Amorphous indium gallium zinc oxide (a-IGZO) has high sensing performance for some oxidizing and reducing gases with low preparation temperature, high carrier mobility, and reduces inhomogeneity of many properties in polycrystalline semiconductor metal oxides due to the lack of grain boundaries. Currently, not much research has been done on a-Ga_2O_3-based gas detectors, mostly using a-IGZO to detect gases such as NO_2, H_2, ozone, ethanol, etc.

In 2011, Zan *et al.*[45] prepared an a-IGZO-based thin-film transistor gas detector in which the organic layer acts as a second gate to form a p–n junction with a-IGZO. When the organic layer comes in contact with oxidizing or reducing gas molecules, the charge transfers between it and the gas molecules lead to a change in potential on the organic layer, which is amplified by the underlying a-IGZO TFT. The gas detector has sensitive and reversible detection of 100 ppb ammonia and 100 ppb acetone at room temperature. In 2012, Yang *et al.*[46] investigated the responsiveness of a-IGZO thin films to oxidizing/reducing gases (NO_2 and H_2) and found that the responsiveness of a-IGZO thin films to both H_2 and NO_2 was comparable to that of polycrystalline semiconductor metal oxides (SMOs) (Fig. 21), and that their simpler structure and lack of grain boundaries allowed them to eliminate many of the electrical, microstructural, and chemical inhomogeneities found in SMOs, making them an ideal material for gas sensor applications.

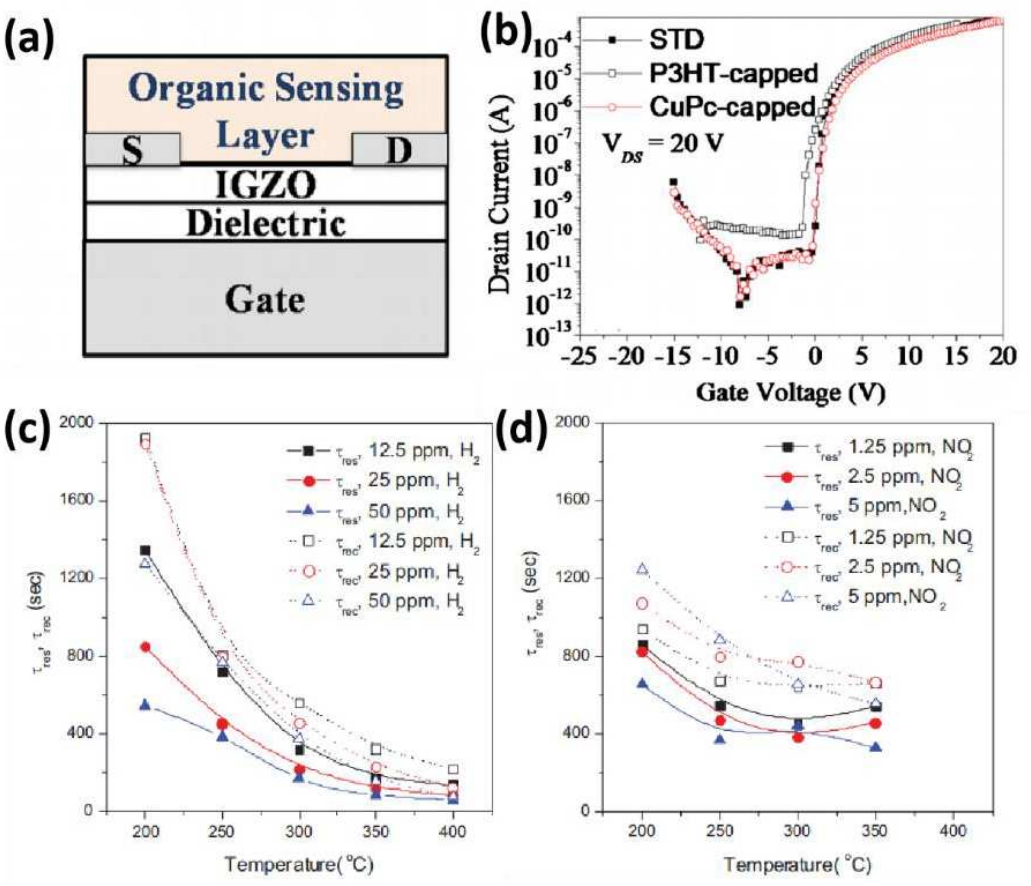


Fig. 21. Temperature dependence of the response/recovery time constants of a-IGZO films for (a) H_2 and (b) NO_2. Reproduced with permission from Ref. [46].

In their experiments, researchers have found a number of ways to optimize the performance of gas sensors. In 2020, Sui *et al.*[47] prepared a room-temperature ozone sensor based on an IGZO-covered a-Ga_2O_3 film, and experimentally confirmed that the sensor responsiveness could be improved by controlling the sputtering time of IGZO. As listed in Table 5, with the increase of sputtering time, the IGZO surface changes from dispersed particles to a complete thin film, and the responsiveness of the sensor exhibits a first increase and then decrease. The analysis shows that the specific surface area of the thin film affects the detection ability of the sensor for ozone to a certain extent. In 2021, Eadi *et al.*[56] prepared NO_2 sensors based on IGZO thin films with ZnO/Ga_2O_3/In_2O_3 stacked structure using ALD and annealed the devices at 500 °C in oxygen atmosphere for 1 h. The annealing made In_2O_3, the top layer of Zn and Ga oxides, more sensitive to NO_2, so the sensing performance of this structure was superior to that of the sensor structure with ZnO as the top layer. Schematic diagrams of the In_2O_3/$ZnGa_2O_4$ stacked structure before and after annealing are shown in Fig. 22. In 2021, Peng and Liu[48] fabricated an amorphous IGZO ethanol gas sensor with Au nanoparticles deposited on the surface to greatly increase the surface area/volume ratio, spillover effect, and catalytic reactivity of Au metal. The ethanol gas sensor was obtained with a response of 465.4 for 2400 ppm C_2H_5OH/air gas at an optimal operating temperature of 250 °C, a response time of 32 s, a recovery time of 21 s, and a minimum detection of 100 ppm C_2H_5OH/air gas.

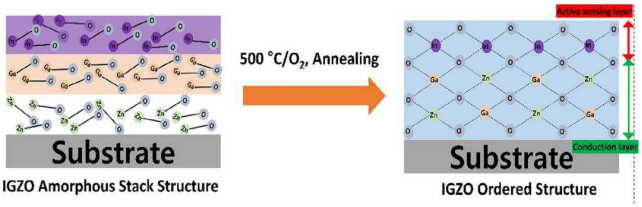


Fig. 22. Schematic diagram of the In_2O_3/$ZnGa_2O_4$ stacked structure and its annealing. Reproduced with permission from Ref. [56].

Table 5. Total photogenerated current density and relative response rate of samples with different IGZO particle sizes with/without ozone input. Reproduced with permission from Ref. [47].

Model	J_{sc}	J'_{sc}	ΔJ_{sc}	S'
$r = 1$ nm particle	0.079541	0.078932	0.000609	1.00772
$r = 2$ nm particle	0.079660	0.078915	0.000745	1.00944
$r = 3$ nm particle	0.080055	0.079013	0.001042	1.01319
$r = 4$ nm particle	0.081022	0.079425	0.001597	1.02011
$r = 5$ nm particle	0.083155	0.080472	0.002683	1.03334
$r = 6$ nm particle	0.088369	0.082415	0.005954	1.07224
$d = 12$ nm thin film	0.097261	0.093514	0.003747	1.04007

4. Conclusion and perspectives

The a-Ga_2O_3 requires less preparation conditions, and a-Ga_2O_3 films can be prepared on rigid or flexible substrates using magnetron sputtering, ALD, PLD, and other methods with growth temperatures ranging from room temperature to 400 °C. In addition, the oxygen vacancy concentration in a-Ga_2O_3 films can be effectively adjusted by annealing, controlling the growth temperature and the oxygen flux during the growth process, thus improving its performance in some specific applications. The a-Ga_2O_3 has excellent photoelectric properties, and this paper reviews a-Ga_2O_3-based photodetectors with various structures such as MSM, Schottky junction, heterojunction and TFT. By adjusting the growth temperature and annealing temperature of the films, the photodetector performance can be improved to a large extent, in which the MSM-type solar-blind UV detector based on annealed a-Ga_2O_3 films can reach a responsivity of 733 A/W. Doping can also change the performance of a-Ga_2O_3 based photodetectors to a certain extent. The doping of In in a-Ga_2O_3 thin film can extend the detection range to 330 nm, and the response rate of Zn-doped a-Ga_2O_3 thin film solar-blind detector can reach 48.99 A/W. Oxygen vacancies play an important role in the resistive switching mechanism of a-Ga_2O_3 based RRAM, and different structures of a-Ga_2O_3 based RRAM are reviewed above, showing that the resistive switching mechanism mostly belongs to the conductive filament theory and space-charge-limited current effect. Finally, gas sensors based on the a-Ga_2O_3 are reviewed. Most of the current studies on a-Ga_2O_3 based gas sensors focus on amorphous indium gallium zinc oxide (a-IGZO) thin films, and IGZO gas sensors can detect gases such as acetone, H_2, NO_2, and ethanol.

As discussed above, a-Ga_2O_3 has applications in many fields due to its unique amorphous structure and simple preparation process. At present, the application of a-Ga_2O_3 in deep-ultraviolet detection has been very mature, and it can continue to be explored in the future to optimize its performance and prepare photodetectors with better self-powered, multi-angle and all-round detection. In RRAM and gas sensors, the applications can be explored more deeply. However, there are still some shortcomings in the application of a-Ga_2O_3. For example, for metal oxides, the intrinsic defects associated with oxygen vacancies are one of the core factors that affect the performance of the material and its devices. The mechanisms of the influence of oxygen vacancies on the physical properties of materials and the performance of their devices are not yet unified, which greatly restricts the optimal preparation and design of a-Ga_2O_3 materials and devices. In future research, theoretical calculations combined with experiments can be used to figure out these problems. Therefore, there is still a long way to go to promote amorphous gallium oxide to be widely used in more military and civil applications.

Acknowledgments

Project supported by the National Key Research and Development Program of China (Grant No. 2022YFB3605404), the National Natural Science Foundation of China (Grant

Nos. 62204126 and 62204125), the Natural Science Research Start-up Foundation of Recruiting Talents of Nanjing University of Posts and Telecommunications (Grant Nos. XK1060921119, XK1060921002, and XK1060921115), and the Open Fund of the Key Laboratory of Aerospace Information Materials and Physics (NUAA) MIIT.

References

[1] Ovshinsky S R 1968 *Phys. Rev. Lett.* **21** 1450
[2] Spear W and Le Comber P 1975 *Solid State Commun.* **17** 1193
[3] Anderson P W 1958 *Phys. Rev.* **109** 1492
[4] Cohen M H, Fritzsche H and Ovshinsky S 1969 *Phys. Rev. Lett.* **22** 1065
[5] Mott N F 1969 *Philos. Mag.* **19** 835
[6] Davis E A and Mott N F 1970 *Philos. Mag.* **22** 0903
[7] Anderson P W 1975 *Phys. Rev. Lett.* **34** 953
[8] Nenashev A V, Oelerich J O, Greiner S H M, Dvurechenskii A V, Gebhard F and Baranovskii S D 2019 *Phys. Rev. B* **100** 125202
[9] Soref R 2006 *IEEE J. Sel. Top. Quantum Electron.* **12** 1678
[10] Hirata A, Yamaguchi R, Kosugi T, Takahashi H, Murata K, Nagatsuma T, Kukutsu N, Kado Y, Iai N, Okabe S, Kimura S, Ikegawa H, Nishikawa H, Nakayama T and Inada T 2009 *IEEE Trans. Microw. Theory Tech.* **57** 1102
[11] Blin S, Tohme L, Coquillat D, Horiguchi S, Minamikata Y, Hisatake S, Nouvel P, Cohen T, Penarier A, Cano F, Varani L, Knap W and Nagatsuma T 2013 *J. Commun. Netw.* **15** 559
[12] Guo D Y, Li P G, Chen Z W, Wu Z P and Tang W H 2019 *Acta Phys. Sin.* **68** 7 (in Chinese)
[13] Dimitrijev S, Han J, Moghadam H A and Aminbeidokhti A 2015 *MRS Bull.* **40** 399
[14] Weyher J L 2006 *Superlattices Microstruct.* **40** 279
[15] Özgür Ü, Hofstetter D and Morkoç H 2010 *Proc. IEEE Inst. Electr. Electron. Eng.* **98** 1255
[16] Chen X, Ren F, Gu S and Ye J 2019 *Photonics Res.* **7** 381
[17] Onuma T, Saito S, Sasaki K, Masui T, Yamaguchi T, Honda T and Higashiwaki M 2015 *JPN J. Appl. Phys.* **54** 112601
[18] Yuan Y, Hao W, Mu W, Wang Z, Chen X, Liu Q, Xu G, Wang C, Zhou H, Zou Y, Zhao X, Jia Z, Ye J, Zhang J, Long S, Tao X, Zhang R and Hao Y 2021 *Fundamental Res.* **1** 697
[19] Liu Z and Tang W 2023 *J. Phys. D: Appl. Phys.* **56** 093002
[20] Du X, Li Z, Luan C, Wang W, Wang M, Feng X, Xiao H and Ma J 2015 *J. Mater. Sci.* **50** 3252
[21] Peng Y, Zhang Y, Chen Z, Guo D, Zhang X, Li P, Wu Z and Tang W 2018 *IEEE Photon. Technol. Lett.* **30** 993
[22] Liu Z, Du L, Zhang S H, Li L, Xi Z Y, Tang J C, Fang J P, Zhang M L, Yang L L, Li S, Li P G, Guo Y F and Tang W H 2022 *IEEE Trans. Electron Devices* **69** 5595
[23] Higashiwaki M, Sasaki K, Murakami H, Kumagai Y, Koukitu A, Kuramata A, Masui T and Yamakoshi S 2016 *Semicond. Sci. Technol.* **31** 034001
[24] Zhou H, Zhang J, Zhang C, Feng Q, Zhao S, Ma P and Hao Y 2019 *J. Semicond.* **40** 011803
[25] Liu Z, Li P G, Zhi Y S, Wang X L, Chu X L and Tang W H 2019 *Chin. Phys. B* **28** 017105
[26] Tak B R, Kumar S, Kapoor A K, Wang D, Li X, Sun H and Singh R 2021 *J. Phys. D: Appl. Phys.* **54** 453002
[27] Kamiya T and Hosono H 2010 *NPG Asia Mater.* **2** 15
[28] Liang H, Han Z and Mei Z 2020 *Phys. Status Solidi* **218** 2000339
[29] Wang J, Xiong Y, Ye L, Li W, Qin G, Ruan H, Zhang H, Fang L, Kong C and Li H 2021 *Opt. Mater.* **112** 110808
[30] Wang Y, Cui W, Yu J, Zhi Y, Li H, Hu Z Y, Sang X, Guo E J, Tang W and Wu Z 2019 *ACS Appl. Mater. Interfaces* **11** 45922
[31] Battu A K and Ramana C V 2018 *Adv. Eng. Mater.* **20** 1701033
[32] Zhang F, Li H, Cui Y T, Li G L and Guo Q 2018 *AIP Adv.* **8** 045112
[33] Cui S, Mei Z, Zhang Y, Liang H and Du X 2017 *Adv. Opt. Mater.* **5** 1700454
[34] Liang H, Cui S, Su R, Guan P, He Y, Yang L, Chen L, Zhang Y, Mei Z and Du X 2018 *ACS Photon.* **6** 351
[35] Zhang Y F, Chen X H, Xu Y, Ren F F, Gu S L, Zhang R, Zheng Y D and Ye J D 2019 *Chin. Phys. B* **28** 028501
[36] Zhu W, Xiong L, Si J, Hu Z, Gao X, Long L, Li T, Wan R, Zhang L and Wang L 2020 *Semicond. Sci. Technol.* **35** 055037
[37] Wang Y, Lo C Y, Wong Y S, Kwok C K G, Shil S K and Yu K M 2021 *J. Alloys Compd.* **875** 160000
[38] Fang M, Zhao W, Li F, Zhu D, Han S, Xu W, Liu W, Cao P, Fang M and Lu Y 2019 *Sensors* **20** 129
[39] Kumar N, Arora K and Kumar M 2019 *J. Phys. D: Appl. Phys.* **52** 335103
[40] Qin Y, Li L H, Yu Z, Wu F, Dong D, Guo W, Zhang Z, Yuan J H, Xue K H, Miao X and Long S 2021 *Adv. Sci.* **8** e2101106
[41] Zhi Y S, Li P G, Wang P C, Guo D Y, An Y H, Wu Z P, Chu X L, Shen J Q, Tang W H and Li C R 2016 *AIP Adv.* **6** 015215
[42] Yang C C, Huang J Q, Chen K Y, Chiu P H, Vu H T and Su Y K 2019 *IEEE Access* **7** 175186
[43] Zhang L, Yu H, Xiong L, Zhu W and Wang L 2019 *J. Mater. Sci.: Mater. Electron.* **30** 8629
[44] Yang Z, Wu J, Li P, Chen Y, Yan Y, Zhu B, Hwang C S, Mi W, Zhao J, Zhang K and Guo R 2020 *Ceram. Int.* **46** 21141
[45] Zan H W, Li C H, Yeh C C, Dai M Z, Meng H F and Tsai C C 2011 *Appl. Phys. Lett.* **98** 253503
[46] Yang D J, Whitfield G C, Cho N G, Cho P S, Kim I D, Saltsburg H M and Tuller H L 2012 *Sens. Actuators B: Chem.* **171** 1166
[47] Sui Y, Liang H, Chen Q, Huo W, Du X and Mei Z 2020 *ACS Appl. Mater. Interfaces* **12** 8929
[48] Peng R Y and Liu W C 2021 *IEEE Trans. Electron Devices* **68** 753
[49] Guo D Y, Wu Z P, An Y H, Li P G, Wang P C, Chu X L, Guo X C, Zhi Y S, Lei M, Li L H and Tang W H 2015 *Appl. Phys. Lett.* **106** 042105
[50] Wang P C, Li P G, Zhi Y S, Guo D Y, Pan A Q, Zhan J M, Liu H, Shen J Q and Tang W H 2015 *Appl. Phys. Lett.* **107** 262110
[51] Siah S C, Brandt R E, Lim K, Schelhas L T, Jaramillo R, Heinemann M D, Chua D, Wright J, Perkins J D, Segre C U, Gordon R G, Toney M F and Buonassisi T 2015 *Appl. Phys. Lett.* **107** 252103
[52] Heinemann M D, Berry J, Teeter G, Unold T and Ginley D 2016 *Appl. Phys. Lett.* **108** 022107
[53] Li X, Yang J G, Ma H P, Liu Y H, Ji Z G, Huang W, Ou X, Zhang D W and Lu H L 2020 *ACS Appl. Mater. Interfaces* **12** 30538
[54] Tao J, Lu H L, Gu Y, Ma H P, Li X, Chen J X, Liu W J, Zhang H and Feng J J 2019 *Appl. Surf. Sci.* **476** 733
[55] Zhou C, Liu K, Chen X, Feng J, Yang J, Zhang Z, Liu L, Xia Y and Shen D 2020 *J. Alloys Compd.* **840** 155585
[56] Eadi S B, Shin H J, Song K W, Choi H W, Kim S H and Lee H D 2021 *Mater. Lett.* **297** 129943
[57] Kelly P J and Arnell R D 2000 *Vacuum* **56** 159
[58] Gudmundsson J T and Lundin D 2020 *High Power Impulse Magnetron Sputtering* (Berlin: Elsevier) p. 1
[59] Zhu J, Xu Z, Ha S, Li D, Zhang K, Zhang H and Feng J 2022 *Materials* **15**
[60] Liu H, Zhou S, Zhang H, Ye L, Xiong Y, Yu P, Li W, Yang X, Li H and Kong C 2022 *J. Phys. D: Appl. Phys.* **55** 305104
[61] Krebs H U, Weisheit M, Faupel J, Süske E, Scharf T, Fuhse C, Störmer M, Sturm K, Seibt M and Kijewski H 2003 *Adv. Solid State Phys.* 505
[62] Zhao J L, Li X M, Bian J M, Yu W D and Gao X D 2005 *J. Cryst. Growth* **276** 507
[63] Leskelä M and Ritala M 2002 *Thin Solid Films* **409** 138
[64] Parsons G N, George S M and Knez M 2011 *MRS Bull.* **36** 865
[65] Xu Y, Cheng Y, Li Z, Feng Q, Zhang Y, Chen D, Zhu W, Zhang J, Zhang C and Hao Y 2021 *Nano Select* **2** 2112
[66] Li S, Yang C, Zhang J, Dong L, Cai C, Liang H and Liu W 2020 *Nanomaterials* **10** 1760
[67] Huang L, Hu Z, Zhang H, Xiong Y, Fan S, Kong C, Li W, Ye L and Li H 2021 *J. Mater. Chem. C* **9** 10354
[68] Chen Y, Lu Y, Liao M, Tian Y, Liu Q, Gao C, Yang X and Shan C 2019 *Adv. Funct. Mater.* **29** 1906040
[69] Zhou H, Cong L, Ma J, Li B, Chen M, Xu H and Liu Y 2019 *J. Mater. Chem. C* **7** 13149
[70] Han Z, Liang H, Huo W, Zhu X, Du X and Mei Z 2020 *Adv. Opt. Mater.* **8** 1901833
[71] Wang Y, Yang Z, Li H, Li S, Zhi Y, Yan Z, Huang X, Wei X, Tang W and Wu Z 2020 *ACS Appl. Mater. Interfaces* **12** 47714
[72] Liu S, Jiao S, Lu H, Nie Y, Gao S, Wang D, Wang J and Zhao L 2022 *J. Alloys Compd.* **890** 161827
[73] Yang L L, Liu Z, Xu Q, Zhang M L, Li S, Guo Y F and Tang W H 2023 *IEEE Sens. J.* **23** 6990
[74] Hong X, Loy D J, Dananjaya P A, Tan F, Ng C and Lew W 2018 *J. Mater. Sci.* **53** 8720